Nano Research

ISSN 1998-0124 CN 11-5974/O4
https://doi.org/10.26599/NR.2026.94908848

Research Article

Iron coordinated by nitrogen doped carbon with dual-iron atom sites derived from binuclear ligand polymer for efficient oxygen reduction reaction

LiZhen Wen[1,2,3], Weiqi Liang[1,2,3], Wanling Xiao[1,2,3], Cunhuai Yu[1,2,3], Jiawang Li[1,2,3], Yunbo Li[1,2,3], ChengFu Tan[1,2,3], Lijuan Wu[1,2,3], Pei Kang Shen[1,2,3], Zhi Qun Tian[1,2,3](✉)

[1] Collaborative Innovation Center of Sustainable Energy Materials, School of Physical Science and Technology, Guangxi University, Nanning 530004, China

[2] Guangxi Key Laboratory of Electrochemical Energy Materials, Nanning 530004, China

[3] State Key Laboratory of Featured Metal Materials and Life-cycle Safety for Composite Structures, Nanning 530004, China

Nano Res., **Just Accepted Manuscript** • https://doi.org/10.26599/NR.2026.94908848

https://www.sciopen.com/journal/1998-0124 on May. 17, 2026

Just Accepted

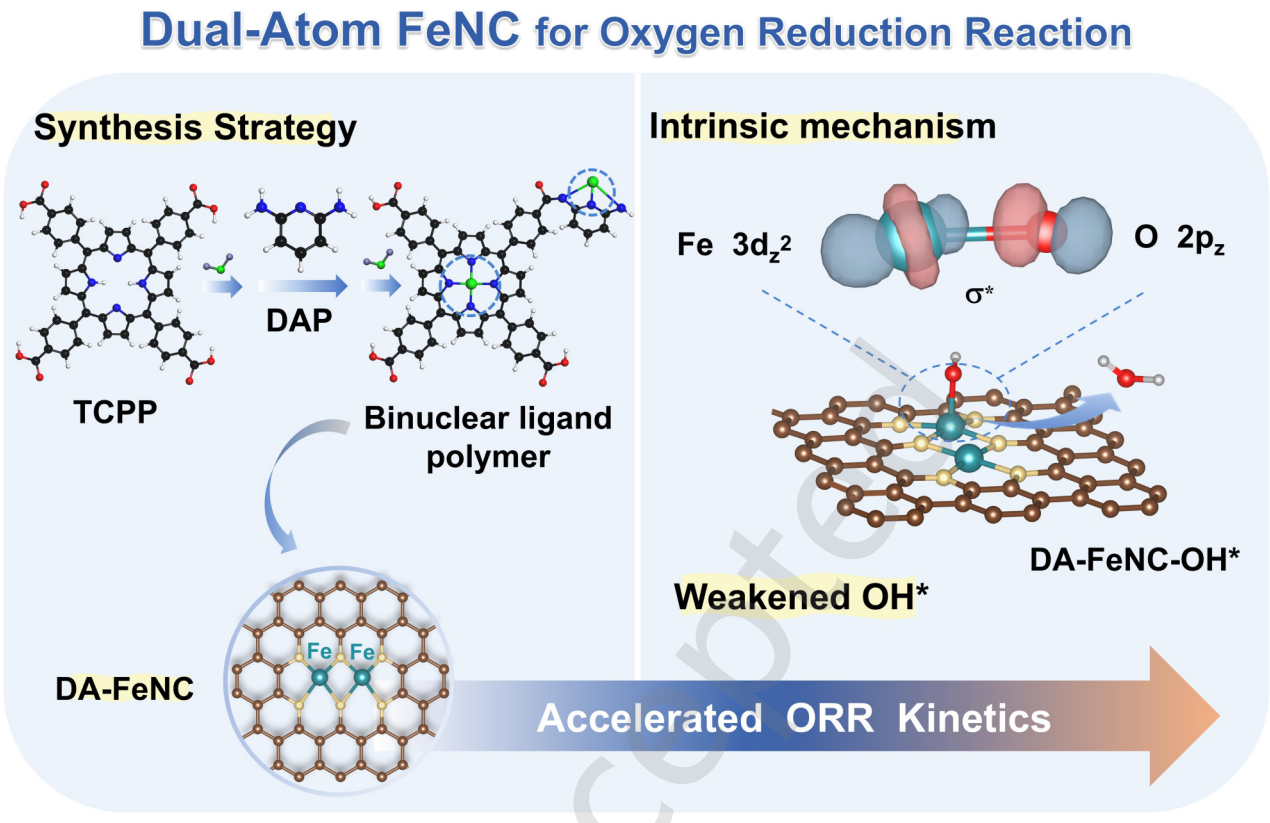

A FeNC with dual-Fe atom sites exhibiting excellent ORR performance in both acidic and alkaline media was precisely fabricated by pyrolyzing a newly designed binuclear ligand polymer synthesized from TCPP and DAP via a condensation reaction.

Nano Research

Open Access

Research Article

Iron coordinated by nitrogen doped carbon with dual-iron atom sites derived from binuclear ligand polymer for efficient oxygen reduction reaction

LiZhen Wen[1,2,3], Weiqi Liang[1,2,3], Wanling Xiao[1,2,3], Cunhuai Yu[1,2,3], Jiawang Li[1,2,3], Yunbo Li[1,2,3], ChengFu Tan[1,2,3], Lijuan Wu[1,2,3], Pei Kang Shen[1,2,3], and Zhi Qun Tian [1,2,3]

[1] *Collaborative Innovation Center of Sustainable Energy Materials, School of Physical Science and Technology, Guangxi University; Nanning 530004, China*

[2] *Guangxi Key Laboratory of Electrochemical Energy Materials, Nanning 530004, China*

[3] *State Key Laboratory of Featured Metal Materials and Life-cycle Safety for Composite Structures, Nanning 530004, China.*

Received: 13 February 2026; **Revised:** 15 April 2026; **Accepted:** 17 May 2026

Address correspondence to tianzhiqun@gxu.edu.cn

Cite this article: *Nano Research*, 2026, 19, 94908848 https://doi.org/10.26599/NR.2026.94908848

ABSTRACT: Breaking the linear scaling relationship of oxygen reduction reaction (ORR) on transition metal coordinated by nitrogen doped carbon (MNC) with single-atom sites is crucial to achieving noble-metal-free fuel cells and metal-air batteries. Herein, FeNC with dual-Fe atom sites (DA-FeNC) was precisely developed by pyrolyzing a newly designed Fe-ion coordination polymer with binuclear ligand precursor, which was copolymerized with meso-Tetra(4-carboxyphenyl)porphine (TCPP) and 2,6-Diaminopyridine (DAP). In the precursor, the porphine in TCPP serves as primary coordination site for Fe ions, and the amide-pyridine ligands generated through the condensation reaction between TCPP and DAP provide secondary Fe ion-coordination site. The resulting DA-FeNC not only delivers high ORR performance with half-wave potentials of 0.82 V in 0.5 M H_2SO_4 and 0.93 V in 0.1 M KOH, and minimal potential losses of 26 mV and 10 mV after 50,000 cycles, respectively, but also achieves a high peak power density of 724 mW cm^{-2} in proton exchange membrane fuel cells and 226 mW cm^{-2} in Zn-air batteries as cathode. Meanwhile, theoretical analyses further indicate that there is a specific electronic coupling effect between adjacent dual-Fe sites in FeNC with more Fe 3d orbital occupancy than that of single-Fe site in FeNC, which increases the population of σ* antibonding states between Fe $3d_{z^2}$ and O $2p_z$ orbitals, reducing the free energy gap of OOH*-OH* to 2.78 eV, effectively breaking the conventional linear scaling limitation of single-Fe atom sites. This work offers an effective strategy for precisely constructing MNCs with dual metal atoms for efficient electrocatalysis of ORR.

KEYWORDS: transition metal coordinated by nitrogen doped carbon, binuclear ligand polymer, oxygen reduction reaction, proton exchange membrane cells, Zn-air batteries

1 Introduction

Nowadays, electrochemical energy conversion technologies have been playing a crucial role in the development of sustainable and green energy supply systems to replace conventional fossil energy. In particular, proton exchange membrane fuel cells (PEMFCs) and metal-air batteries have received wide attention due to their high energy efficiency, sustainability, and zero emissions [1, 2]. In these devices, the cathodic oxygen reduction reaction (ORR) via a four-electron transfer pathway occupies a predominant position in determining the overall efficiency [3-5]. Currently, Pt-based catalysts with low ORR overpotential are usually employed to achieve the desired power output [6]. Unfortunately, the limited global reserves of Pt resources pose a critical obstacle to their widespread adoption [7, 8]. Consequently, there is an urgent need to develop efficient non-precious metal electrocatalysts for the ORR.

Transition metal coordinated by nitrogen doped carbon (MNC) have been regarded as the most promising candidate to replace the current Pt-based catalysts for ORR, due to their high atomic utilization, strong metal-support interactions, and unique electronic structures [9]. Generally, the active sites in MNC for ORR are associated with MN_x moieties featuring atomically dispersed transition metal centers coordinated by nitrogen atoms doped into carbon substrates [10-12]. So far, numerous MNCs based on various transition metals, including Fe, Co, and Mn et. al, have been reported as promising candidates for the ORR [13-16]. Furthermore, the introduction of heteroatoms (e.g., B, N, S, P) into the carbon matrix or the adjustment of coordinating atoms with them has been shown to further modulate the electronic structure of the central metal atoms, thereby improving ORR activity [17-19]. Among MNCs, FeNC exhibits the highest ORR activity, but its performance under practical conditions is still inferior to that of Pt-based catalysts [20]. This limitation arises mainly from weak interactions between isolated metal atoms and the inherent linear scaling

relationship of oxygen intermediate adsorption/desorption, ultimately restricting both the catalytic activity and kinetics of the ORR [21]. To address this challenge, dual-atom Fe-based catalysts featuring two adjacent metal atoms as active sites have been recently proposed. As an extension of single-metal site catalysts, Fe-based dual-metal center catalysts not only inherit the advantages of FeNC but also offer additional features, including cooperative effects, geometric effects, and electronic ligand effects [22, 23]. To date, a variety of strategies have been developed to construct Fe-based dual-metal center catalysts [24, 25]. For example, the formation of dual-atom sites can be promoted by confining metal precursors within zeolitic imidazolate frameworks (ZIF-8) and increasing the loading amount of metal precursors [26, 27]. In addition, the use of metal dimer precursors can enhance the pairing ratio of dual-atom sites [28-30]. Moreover, defect engineering around FeN_x sites was developed as anchoring points for secondary metal atoms [31, 32]. These strategies have greatly advanced the development of dual-atom MNCs. However, their formation generally relies on anchoring additional metal ions or FeN_x fragments into N-doped carbon supports, leading to relatively weak interactions between the metal active sites and the carbon substrate, which ultimately undermines structural integrity and long-term stability. Therefore, it is highly desirable to realize the molecular-level construction of a stable dual-metal MNC for highly efficient ORR catalysis by further developing synthetic strategies with precise controllability.

In this work, we report a viable strategy of precisely constructing FeNC featuring dual-Fe atom centers (DA-FeNC) for efficient ORR performance in both acid and alkaline media, which was achieved through pyrolyzing a newly designed dual-Fe ion coordinated polymer, synthesized from meso-tetra(4-carboxyphenyl)porphine (TCPP) and 2,6-diaminopyridine (DAP) via a condensation reaction. In the precursor, the porphine in the TCPP acts as the primary coordination center for Fe ions, while the secondary coordination centers are composed of the amide groups generated via the condensation together with pyridine in the DAP. Attributed to the specific precursor design with two ligands with Fe ions, FeNC with dual Fe atoms can be precisely synthesized. Meanwhile, compared with FeNC with single-Fe sites, dual-Fe sites in DA-FeNC have a specific cooperative electronic coupling with more Fe 3d orbital occupancy, which downshifts the d-band center, enhancing the occupation of σ* antibonding states of Fe $3d_{z^2}$ and O $2p_z$ orbitals, breaking the conventional linear scaling relationship of ORR occurring on the single Fe site. As a result, the DA-FeNC with the Fe atomic distance of around 2.7 Å exhibits exceptional ORR performance with half-wave potentials ($E_{1/2}$) of 0.82 V and 0.93 V (vs. RHE) and minimal degradation losses of 26 and 10 mV after 50,000-cycle durability test in acidic and alkaline media, respectively, outperforming the single-atom FeNC (SA-FeNC). Moreover, when evaluated in a practical PEMFC and Zn-air battery, it delivers high peak power densities of 724 mW cm^{-2} and 226 mW cm^{-2}, respectively. These results demonstrate that the strategy of constructing dual-atom MNCs based on the new precursor of binuclear ligand amide polymer provides an effective route for developing dual-atom MNCs with advanced ORR performance.

2 Experimental Section

2.1 Synthesis of FeNCs with dual Fe atom active sites

In the typical synthesis of Fe-N-C with dual Fe atom sites, 0.5 mmol of meso-Tetra(4-carboxyphenyl)porphine (TCPP)and 0.5 mmol of $FeCl_2{\cdot}4H_2O$ were first dissolved in 10 mL of ethanol under stirring to form an Fe ion-coordinated complex by TCPP (TCPP-Fe). Next, the dark green solution was mixed with 15 g of NaCl in a 100 mL agate jar by a ball-mill process at 500 rpm for 12 h. After that, 1.0 mmol of 2,6-Diaminopyridine (DAP) dissolved in 10 mL of ethanol was introduced into the jar and subjected to one more 12 h ball-milling process in the presence of 100 mg of oxalic acid as the catalyst to form the copolymer of TCPP and DAP (TCPP-Fe-DAP), while specific Fe-ion tridentate ligands consisting of two amide bonds (-CO-NH-) derived from the condensation of carboxyl group in TCPP and amino group in DAP as well as the pyridine in DAP were synthesized. Subsequently, another 0.5 mmol of $FeCl_2{\cdot}4H_2O$ in 10 mL of ethanol was added to the polymer precursor, and the ball milling process was continued for 12 h to obtain the Fe ion dual-ligand coordination polymer (TCPP-Fe-DAP-Fe). The dried precursor with NaCl was then pyrolyzed at 900 ℃ for 1 h in N_2 and followed by acid treatment in 0.5 M H_2SO_4 at 80 ℃ and stirred continuously for 10 h to remove unstable Fe species. After drying, the black product underwent a secondary calcination treatment at 900 ℃ to obtain the final sample. The Fe-N-C synthesized by the procedure was named as dual-atom FeNC (DA-FeNC). For comparison, FeNC with a single-Fe atom (SA-FeNC) was synthesized by the same method but without the second Fe^{2+} addition. Meanwhile, N-doped carbon (NC) was also prepared by using the polymer precursor without adding Fe ions.

2.2 Characterizations

The copolymerization of TCPP and DAP with the formation of amide bonds was verified by a Fourier Transform Infrared Spectrometer (FTIR, VERTEX 70). Field-emission scanning electron microscopy (FESEM, Hitachi SU 8220), high-resolution transmission electron microscopy (HRTEM, JEOL JEM-2100), and aberration-corrected high-angle annular dark field scanning transmission electron microscopy (AC-HAADF-STEM, Titan Cubed Themis G2 300) were used to characterize the morphologies, carbon structures, and Fe atom distributions of the samples, respectively. The crystalline structures of the samples were analyzed using X-ray diffraction (XRD, Bruker D8-Advanced diffractometer) with Cu-Kα irradiation source (λ = 1.5406 Å). Meanwhile, a Raman spectrometer (Lab RAM HR Evolution) was employed to detect the defects of the carbon matrix in the samples. N_2 adsorption/desorption isotherms of the samples were measured using the Micromeritics ASAP 2460 instrument at 77 K. To reveal the composition and chemical states of the samples, X-ray photoelectron spectroscopy (XPS) measurements were performed on an ESCALAB 250 system. The coordinative structures of Fe atom and N dopants in the samples were identified by X-ray fine absorption spectroscopy (XFAS) experiments at the XAFCA beamline of the Singapore Synchrotron Light Source.

2.3 Electrochemical measurements for ORR

The ORR electrochemical performance of DA-FeNC and SA-FeNC was measured in a standard three-electrode cell connected with the PINE system. In the cell, a rotating ring disk glassy electrode (0.2475 cm^2 area) coated with the sample served as the work electrode, a graphite rod and a commercial reversible hydrogen electrode (RHE) were used as the counter electrode and the reference electrode, respectively. The working electrode was prepared by using the following process: 5 mg of FeNC was homogenously dispersed into 500 μL of mixed solution with 400 μL of anhydrous ethanol, 80 μL of H_2O, and 20 μL of Nafion (5 wt%) to form a uniform ink. After that, the prepared ink was dropped on the working electrode and dried naturally to achieve the sample loading of 600 μg cm^{-2}. Meanwhile, an electrode with a Pt loading of 50 μg_{Pt} cm^{-2} was also prepared using a commercial Pt/C catalyst (46.7 wt%, TKK) for comparison. In the electrochemical measurements, all the tests were conducted in a 0.5 M H_2SO_4 (0.1 M KOH) that bubbled with O_2 or N_2 for at least 30 min before the measurement. To achieve reliable and reproducible ORR performance of FeNCs, all the working electrodes were first activated by cyclic voltammetry (CV) with a potential range between 0.05 and 1.1 V vs. RHE until stable CV curves were reached. After that, ORR performance was measured by linear scanning voltammetry (LSV) tests in a potential range from 1.1 V to 0 V vs. RHE at a scan rate of 5 mV s^{-1} and a rotating rate of 1600 rpm.

Turnover frequency (TOF) of the DA-FeNC and SA-FeNC were determined by the following equation (Eq. (1)):

$$TOF[\text{e site } s^{-1}] = \frac{\left|j_k^{unpoisoned} - j_k^{poisoned}\right| [mA\ cm^{-2}] \times N_A [mol^{-1}]}{m_c [mg\ cm^{-2}] SD_{mass} [site\ g^{-1}] \times F [A\ s\ mol^{-1}]} \quad (1)$$

Where j_k is the kinetic current at the unpoisoned and poisoned states, m_c is the catalyst loading (0.27 mg cm^{-2}), N_A is Avogadro constant, SD_{mass} is mass-normalized site density of the catalyst, and F is the Faraday constant.

2.4 Fabrication of a single proton exchange membrane fuel cell (PEMFC) and Zn-air battery and tests

As for the PEMFC, the cathode was prepared by spraying the ink containing 60.0 mg of FeNC, 10.0 mL of isopropanol, 2.0 mL of H_2O, and 240.0 mg of Nafion solution (25.0 wt%) onto the Gore membrane (M788.12, Sinero, 4.84 cm^2). The cathode catalyst loading was 3.0 mg cm^{-2}. Meanwhile, the commercial Pt/C (46.7 wt%, TKK) cathode with a Pt loading of 0.05 mg_{Pt} cm^{-2} and the anode with 0.2 mg_{Pt} cm^{-2} were prepared by the same procedure. Finally, a membrane electrode assembly (MEA) was fabricated by placing a GORE (M788.12, Suzhou Sinero Technology Co., Ltd) between the cathode and anode, followed by a hot-pressing at 135 ℃ under 25 kgf for 120 s. The MEA performance was evaluated using a Scribner 850e fuel cell test station under a pressure of 150 kPa and at 80 ℃, with 100% humidified hydrogen and oxygen supplied at flow rates of 500 and 2000 mL min^{-1}, respectively. The durability tests were carried out by cycling the voltage from the open-circuit voltage to 0.1 V at a scan rate of 0.02 V s^{-1}.

For the fabrication of a Zn-air battery, the cathode was prepared by the following steps: 10 mg of FeNC was dispersed ultrasonically into a mixture consisting of 800 μL of anhydrous ethanol, 160 μL of H_2O, and 40 μL Nafion (5 wt%). The FeNC ink was uniformly dropped onto a circular gas diffusion layer (H24XC483, Gatechn New Energy Technology Co., Ltd) with an active area of 0.785 cm^2, resulting in a catalyst loading of 0.60 mg cm^{-2}. Subsequently, the Zn-air battery was fabricated by assembling the prepared cathode into a home-made Teflon cell with a polished zinc plate (with a thickness of 0.3 mm) serving as the anode. The electrolyte was composed of 6.0 M KOH and 0.2 M zinc acetate. For comparison, the Pt/C electrode with the same catalyst loading was also prepared. The battery performance was measured by using LSV with an O_2 flow rate of a scan rate of 20 mV s^{-1} at room temperature. The specific capacity of the battery was evaluated at a current density of 10 mA cm^{-2}.

2.5 Computational Details

To elucidate the in-depth mechanism of FeNCs with single and dual Fe atom active sites for ORR at the atomic level, density functional theory (DFT) calculations were performed [33]. First, the dual-atom FeNC and single-atom FeNC models with a 5 × 3 graphene supercell were constructed in Materials Studio, and a vacuum spacing of 15 Å in the z-direction was applied to avoid periodic interactions. In the work, all DFT calculations were carried out using the Vienna Ab initio Simulation Package (VASP) [34], in which the exchange-correlation effects were described by the Perdew-Burke-Ernzerhof (PBE) functional within the generalized gradient approximation (GGA) [35], and the projector augmented wave (PAW) pseudopotentials were employed to treat the interactions between nuclei and valence electrons.[34] Meanwhile, to accurately describe possible weak interactions in the system, the DFT-D3 method was included for dispersion correction [36]. and Brillouin zone sampling was performed only at the Γ point using a 1×1×1 Monkhorst-Pack k-point mesh [37]. Moreover, the Kohn-Sham wavefunctions were expanded in a plane-wave basis set with a cutoff energy of 400 eV. All atomic positions were fully relaxed until the Hellmann-Feynman forces on each atom were below 0.01 eV/Å and the electronic self-consistency loop was converged to lower than 1×10^{-5} eV.

3 Results and Discussion

3.1 Synthesis and structural characterization of FeNCs with single and dual Fe atom sites

Figure 1 illustrates the precise synthetic route of SA-FeNC and DA-FeNC via a specifically designed Fe ion coordination polymer with binuclear ligand as precursor based on the copolymerization of TCPP and DAP via a simple condensation reaction. In the design, the porphine in the TCPP served as the primary ligand is initially mixed with the Fe salt to form the TCPP-Fe complex. Subsequently, the amide bonds formed between TCPP (-COOH) and DAP ($-NH_2$) together with the pyridine in DAP construct a tridentate ligand, providing secondary complexation sites for Fe ions. After adding one more Fe ion, the resulting Fe-containing polymers are then subjected to high-temperature pyrolysis under N_2. After acid leaching to remove unstable Fe species, followed by a second annealing step, the DA-FeNC is finally synthesized. Correspondingly, the SA-FeNC is synthesized by using the precursor with only Fe coordinated by TCPP. In addition, the successful copolymerization of TCPP and DAP

is evidenced by FTIR detection with the formation of amide groups and disappearance of carbonyl groups in TCPP and ammonia in DAP after reaction (**Figure S1**). Meanwhile, the capability of the copolymer of TCPP and DAP with binuclear

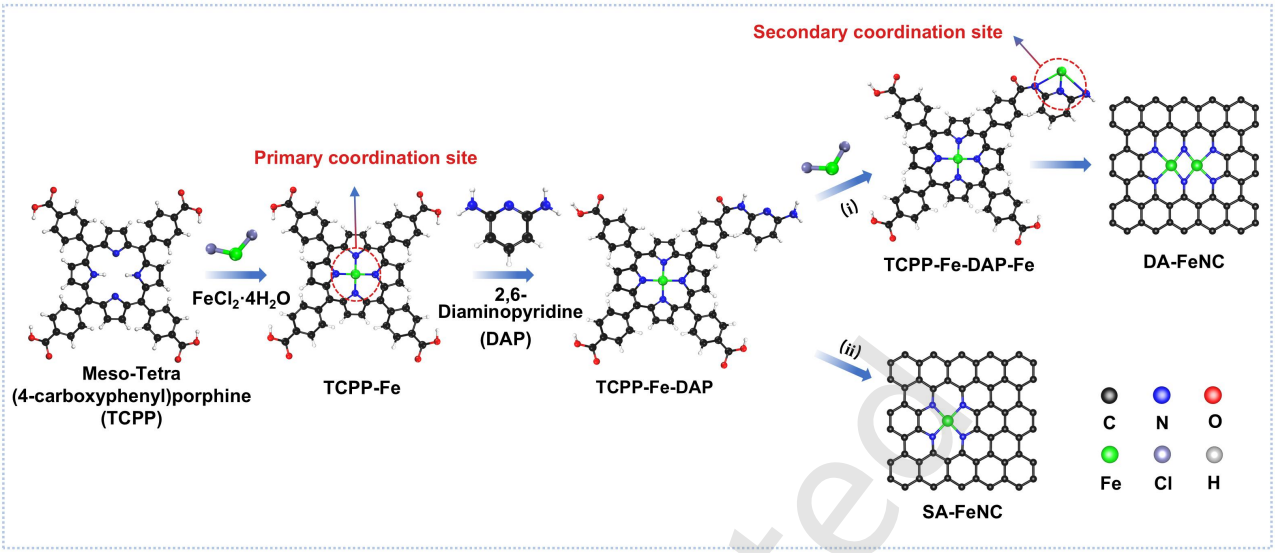

Figure 1 Schematic diagram of synthesizing FeNCs with single and dual Fe atoms by pyrolyzing the Fe ion dual-ligand coordination polymer.

ligand for coordinating Fe ions is confirmed by XPS with an obvious shift of N 1s and Fe 2p before and after introducing Fe ions into the polymer (**Figure S2**).

Figure 2 shows the structural characteristics of DA-FeNC and SA-FeNC, which were synthesized by introducing Fe ions into the precursor twice and once, respectively. The TEM image in **Figure 2a** and the SEM image in **Figure S3** show that the DA-FeNC has a three-dimensional (3D) graphene-like structure, which is composed of cross-linked ultrathin nanosheets. Through further observation by HRTEM (**Figure 2b**), the nanosheets in DA-FeNC are filled with highly curved and distorted graphite lattices, exhibiting the characteristic features of hard carbon [38]. The formation of specific graphite lattices should be closely related to the amide-linked precursor, which generates oxygen-containing gases during pyrolysis, effectively disrupting the original graphite lattices. Meanwhile, it is found that a homogeneous distribution of Fe, N, C, and O elements is observed throughout the nanosheets (**Figure 2c-d**). To identify the Fe atom distributions in the sample at the atomic scale, three regions marked by squares in the AC-HAADF-STEM image (**Figure 2e**) were further observed. As shown in **Figure 2g-i**, Fe atoms appear as abundant paired bright spots (highlighted by orange circles) in DA-FeNC, indicating the presence of dual-Fe atom sites. A statistical analysis based on multiple regions, reveals that dual-Fe sites account for approximately 77.7% of the total Fe species, while isolated single-Fe sites only contribute 22.3% (**Figure S4**). And these bright spots correspond to Fe atoms, which are surrounded by C and N atoms, revealed by electron energy loss spectroscopy (EELS) analysis shown in **Figure 2f**. In contrast, the SA-FeNC obtained by only adding Fe ions into the precursor to coordinate TCPP with a similar nanosheet morphology (**Figure S5**) displays a random distribution of isolated single Fe atoms (**Figure 2j**). Moreover, the magnified 3D atom-overlapping Gaussian-function fitting maps (**Figure 2k-l**) further illustrate the difference between the paired nature of Fe atoms in DA-FeNC and the isolated configuration in SA-FeNC, in which the distances between neighboring Fe atoms in DA-FeNC are 0.264 nm and 0.273 nm, which is far shorter than that of the atomic distance between isolated Fe atoms in SA-FeNC (0.507 nm), indicating the successful formation of dual Fe atom sites. To further reveal the critical role of second complexing sites constructed by two amide bonds and pyridine in DAP for the specific DA-FeNC, m-Phenylenediamine (MPD) was used to react with TCPP instead of DAP for the synthesis of the Fe ion-coordinated polymer precursor, as shown in **Figure S6a**. The TEM image (**Figure S6b**) and the AC-HAADF-STEM image (**Figure S6c**) of SA-FeNC-MPD show that isolated Fe atomic sites are randomly distributed on the nanosheets, which is similar to those observed in SA-FeNC. The results strongly demonstrate that integrating the TCPP macrocycle with amide and pyridinic N coordination units is crucial for constructing stable dual-atom metal sites.

To investigate the chemical states of elements in SA-FeNC and DA-FeNC, XPS was performed. The XPS full-scan survey spectra (**Figure S7**) show the presence of C, N, and Fe elements in both SA-FeNC and DA-FeNC, and **Table S1** summarizes the elemental compositions, with Fe contents of 0.24 at% and 0.53 at% for SA-FeNC and DA-FeNC, respectively. Moreover, the Fe mass contents measured by inductively coupled plasma optical emission spectrometry (ICP-OES) are 1.52 wt% and 2.95 wt%, respectively. The ratio of Fe content in DA-FeNC to SA-FeNC is approaching 2.0, further reflecting that precise synthesis of FeNC with single and dual-Fe atom sites was achieved through the specific design developed in this work. In the high-resolution C 1s spectra (**Figure S8**), five deconvolved components are located at 284.68 eV, 285.50 eV, 287.06 eV, 288.89 eV, and 290.70 eV, corresponding to graphitic C=C (sp^2), defective peak C-C (sp^3), C-N, C=O/C=N, and π^*-π^* [39]. The sp^3/sp^2 ratio of DA-FeNC is 0.50, which is higher than that of SA-

FeNC (0.43), indicating that incorporating the second Fe site generates more defects. Meanwhile, **Figure 3a** shows the high-resolution N 1s spectra, in which four peaks can be fitted,

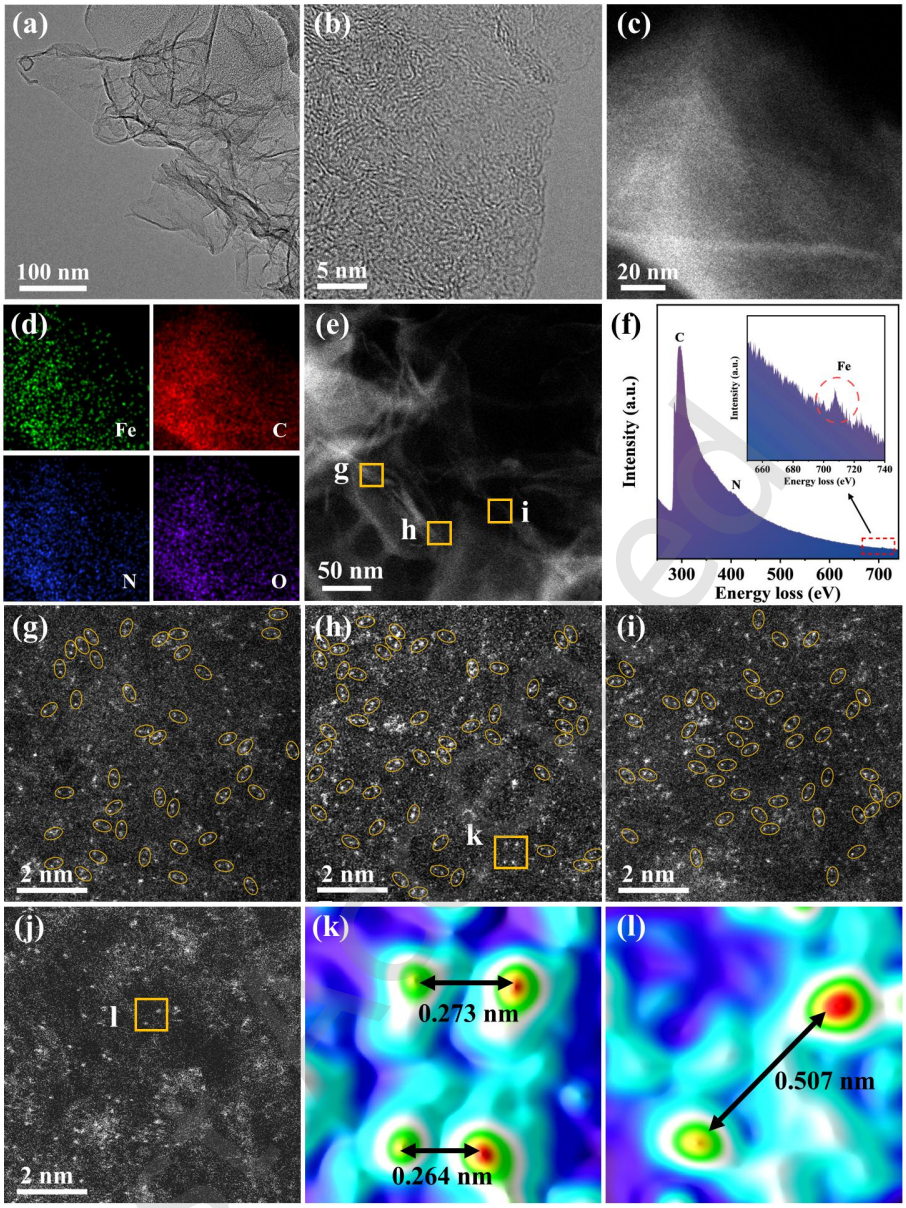

Figure 2 (a) TEM image, (b) HRTEM image, (c, d) elemental mapping images, (e) HAADF-STEM, (f) electron energy loss spectroscopy (EELS) and elemental maps, and (g-i) AC-HAADF-STEM image of DA-FeNC; (j) AC-HAADF-STEM image of SA-FeNC; 3D atom-overlapping Gaussian-function fitting map of (k) DA-FeNC in the regions marked by a yellow square i, and (l) SA-FeNC in j.

corresponding to pyridinic-N (398.5 eV), pyrrolic-N (399.8 eV), graphitic-N (401.0 eV), and oxidized-N (402.5 eV), respectively [40]. As shown in **Table S2**, the dominant N species of DA-FeNC is pyridinic-N, accounting for 43.77%, followed by graphitic-N (35.78%), pyrrolic-N (15.11%), and oxidized-N (5.34%). In contrast, SA-FeNC has graphitic-N (39.29%), pyridinic-N (34.50%), pyrrolic-N (17.80%), and oxidized-N (8.41%). This difference indicates that the introduction of the secondary Fe site significantly alters the distribution of N species. Furthermore, Fe 2p spectra (**Figure 3b**) show that DA-FeNC exhibits two distinct peaks at 710.78 eV and 723.81 eV, corresponding to Fe $2p_{3/2}$ and Fe $2p_{1/2}$, respectively [41], and the peaks at 716.34 eV and 730.78 eV can be attributed to the satellite peaks [42]. Notably, compared with those of SA-FeNC, the binding energy of Fe $2p_{3/2}$ and Fe $2p_{1/2}$ in DA-FeNC exhibit slight negative shifts of 0.11 eV and 0.19 eV, respectively, indicating a decreased oxidation state of Fe. These results suggest that the electronic structure of Fe in DA-FeNC is markedly different from that in SA-FeNC, thereby exerting a crucial influence on the overall catalytic performance for ORR.

The local structural information of Fe in these samples was further probed by XAS, using Fe foil, FeO, Fe phthalocyanine (FePc), and Fe_2O_3 as standard references. The normalized Fe K-edge X-ray absorption near-edge structure (XANES) spectra (**Figure 3c**) demonstrate that the absorption edge positions of SA-FeNC and DA-FeNC are located between those of FeO and Fe_2O_3, implying that the Fe centers exhibit valence states between +2 and +3. Furthermore, DA-FeNC exhibits a negative energy shift relative to SA-FeNC, suggesting that the introduction of the secondary Fe site reduces the Fe valence state, which is in agreement with the XPS results. In the extended X-ray

absorption fine structure (EXAFS) spectra (**Figure 3d**), a dominant peak is observed at ≈1.45 Å for SA-FeNC and DA-FeNC, which is close to the Fe-N bond in FePc, corresponding to the Fe-N scattering path of the first shell [30]. Notably, a secondary peak is observed in the DA-FeNC spectra at ≈ 2.38

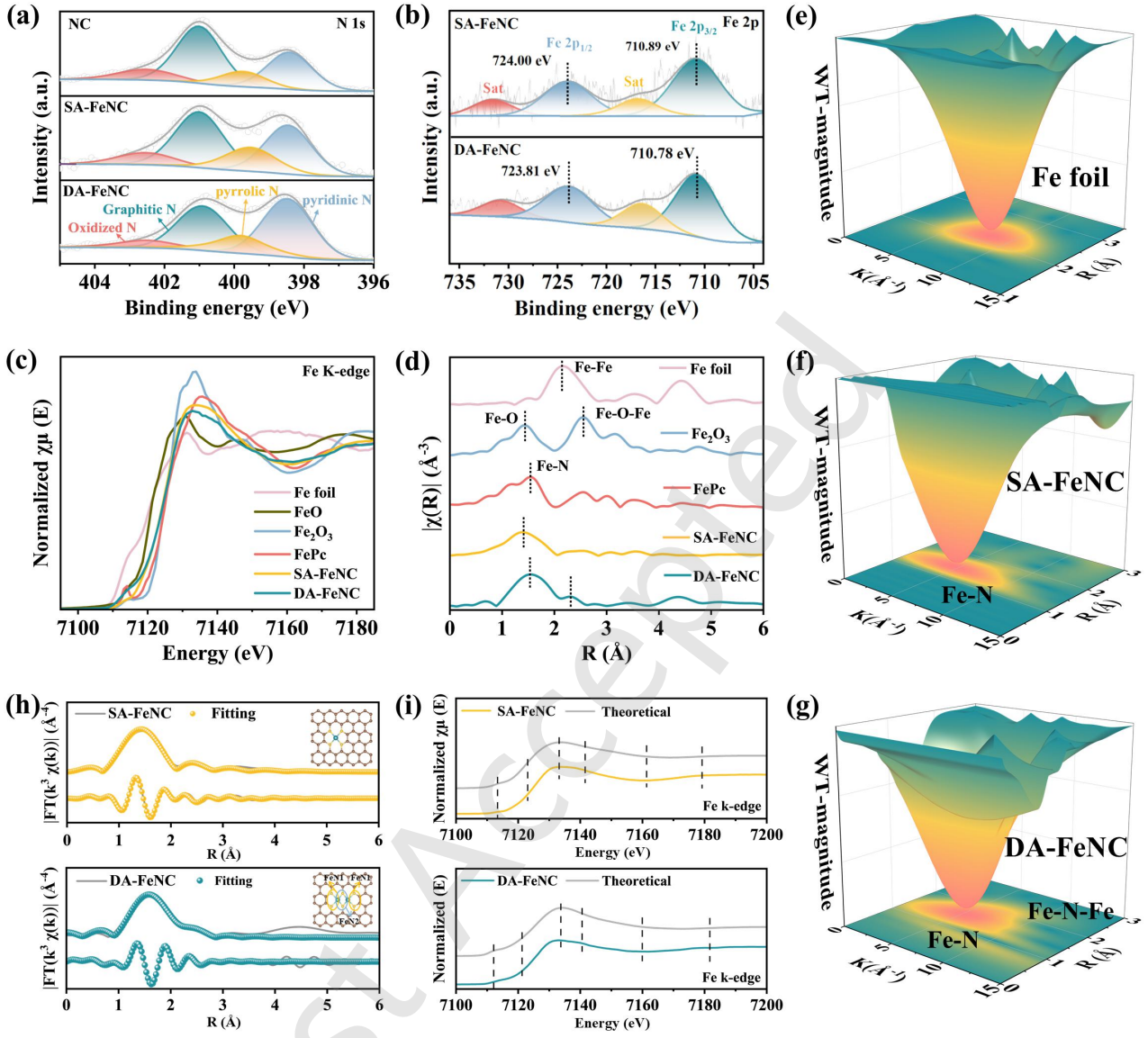

Figure 3 (a) XPS N 1s spectra and (b) XPS Fe 2p spectra of NC, SA-FeNC, and DA-FeNC; (c) k-dege XANES spectra and d) FT-EXAFS spectra of SA-FeNC, and DA-FeNC and the standards of Fe foil, FeO, Fe_2O_3, and FePc; Wavelet transformed EXAFS of (e) Fe foil, (f) SA-FeNC, and (g) DA-FeNC; (h) Fourier transformed K3-weighted (k)-function of SA-FeNC and DA-FeNC; (i) Comparisons between the experimental K-edge XANES spectra and the theoretical spectra based on the corresponding optimized structures for SA-FeNC and DA-FeNC.

Å, which is longer than the Fe-Fe distance of ≈2.16 Å in the Fe foil. This observation is indicative of the existence of neighboring Fe atoms in DA-FeNC [43, 44]. To visually reveal the differences in the local coordination environments between DA-FeNC and SA-FeNC, wavelet transform (WT) analysis was performed. As depicted in **Figure 3e-g**, the WT-EXAFS spectra of DA-FeNC and SA-FeNC exhibit a maximum in k-space at ≈5Å^{-1} and a maximum in R-space at ≈1.5 Å, which is similar to that of FePc (**Figure S9**), indicating that these features are attributable to Fe-N interactions. In contrast, the Fe foil exhibits a higher maximum in k-space at ≈ 8Å^{-1} and a higher maximum in R-space at ≈ 2.2 Å, attributable to the metallic Fe-Fe scattering path. Notably, the secondary scattering feature in DA-FeNC is observed at slightly higher R values (R > 2.0 Å), which is assigned to the Fe-N-Fe multiple scattering associated with the dual-Fe sites configuration rather than long-range Fe-C/N scattering. These findings provide strong evidence that the Fe atoms in the boths samples are atomically dispersed. Additionally, the fitting results of the Fe K-edges using Demeter reveal that the Fe atoms in SA-FeNC exhibit the typical FeN_x moiety configuration with a coordination number of 4.0 and a Fe-N bond length of 1.97 Å (**Figure 3h** and **Table S3**). For DA-FeNC, there are two sites with Fe-N coordination numbers of 4 and Fe-N bond lengths of 2.04 and 1.93, respectively (**Figure 3h** and **Table S3**). Moreover, the fitted coordination number of the Fe-Fe bond is 1.0, with a corresponding bond length of 2.58 Å, which is close to 2.7 Å for the Fe pair atomic spacing measured in the HAADF-STEM image (**Figure 2k**), further confirming the existence of neighboring dual-Fe sites. Furthermore, to validate the structure, theoretical simulations of the Fe K-edge XANES spectra were performed

using the FDMNES code based on the VASP-optimized Fe_2N_6 structure. The calculation results are in excellent agreement with the experimental data, further validating the reliability of the scattering path assignment in the XANES analysis (**Figure 3i**). These results further support the use of binuclear ligand polymer as effective precursors for the rational design of DA-FeNC catalysts.

On the other hand, **Figure S10** shows the XRD patterns of DA-FeNC and SA-FeNC, wherein two broad diffraction peaks are observed around 24.5° and 43°, which can be assigned to the (002) and (101) planes of the graphite-2H phase (PDF#41-1487), respectively [45]. The negative shift at the (002) plane should be due to the twist of the graphitic lattices. Notably, no diffraction signals corresponding to Fe-based species are detected, thereby excluding the presence of Fe nanoparticles [46]. Moreover, Raman spectra in **Figure S11** clearly display two characteristic carbon peaks at 1610 cm^{-1} and 1370 cm^{-1}, which correspond to the graphitic band (G) and the disordered band (D), respectively [47]. To obtain more details, the D peak was further divided into three bands using a Gaussian fitting, in which the D_1 band at round 1370 cm^{-1} corresponds to disordered or defective structures within the carbon lattice and at its edges, the D_2 band at 1520 cm^{-1} arises from distortions induced by pentagons or heteroatoms and the D_3 peak at 1200 cm^{-1} is assigned to polyene-like structures or ionic impurities [48]. In addition, the highest peak intensity ratio (I_{D1}/I_G) and peak area ratio (A_{D1}/A_G) indicate the degree of defect and disorder. The I_{D1}/I_G values are 0.93 (NC), 1.07 (SA-FeNC), and 1.12 (DA-FeNC), and the A_{D1}/A_G values are 1.47, 1.62, and 1.87, respectively, confirming that the degree of defects increases with the incorporation of Fe at the secondary sites (**Table S4**).

Figure S12a shows N_2 adsorption-desorption isotherms of NC, SA-FeNC, and DA-FeNC. All samples exhibit typical type-IV hysteresis loops, indicating they are mesoporous and microporous [49]. The Brunauer-Emmett-Teller (BET) surface area of DA-FeNC is 244.0 $m^2\ g^{-1}$, which is higher than that of NC (100.8 $m^2\ g^{-1}$) and SA-FeNC (133.3 $m^2\ g^{-1}$). Furthermore, the pore size distribution curves (**Figure S12b**) reveal that all three samples possess a hierarchical porous structure, encompassing micro-, meso-, and macropores. To further clarify the distribution of different pore structures, the pore volumes were systematically analyzed. As shown in **Table S5**, the Barrett-Joyner-Halenda (BJH) total pore volumes of NC, SA-FeNC, and DA-FeNC are 0.1793 $cm^3\ g^{-1}$, 0.2700 $cm^3\ g^{-1}$, and 0.3623 $cm^3\ g^{-1}$, respectively. DA-FeNC exhibits the largest total pore volume, as well as the highest absolute volume across micropores (0.09 $cm^3\ g^{-1}$), mesopores (0.16 $cm^3\ g^{-1}$), and macropores (0.11 $cm^3\ g^{-1}$). Notably, the introduction of the first Fe site (SA-FeNC) only slightly increases the micropore fraction (16.6% vs. 16.0% for NC), whereas the addition of the second Fe site (DA-FeNC) significantly enhances microporosity to 24.9%. These results indicate that the NaCl template primarily facilitates the formation of mesopores and macropores, while Fe species, particularly the second Fe coordination site, play a crucial role in micropore generation, synergistically constructing the hierarchical pore structure. In this structure, micropores effectively expose Fe active sites, while the abundant mesopores and macropores facilitate mass transport, thereby enhancing active site accessibility and utilization during the ORR process and contributing to the formation of efficient triple-phase boundaries in PEMFC cathodes.

3.2 Electrochemical Activity of the FeNCs with single and dual atoms for ORR

Figure 4a shows the ORR LSV curves of NC, SA-FeNC, DA-FeNC, and commercial Pt/C in O_2-saturated 0.5 M H_2SO_4 solution. DA-FeNC exhibits a significantly higher ORR activity with a half-wave potential ($E_{1/2}$) of 0.82 V νs. RHE than those of NC (0.58 V νs. RHE) and SA-FeNC (0.78 V νs. RHE), which is comparable to commercial Pt/C (0.83 V νs. RHE). Meanwhile, their corresponding average electron transfer number (n) and the H_2O_2 yield are shown in **Figure 4b**, in which DA-FeNC delivers an exceptionally low H_2O_2 yield (< 1%) and a near-ideal n value of 3.98-3.99, which is approaching those of Pt/C (< 3%, 3.95-3.99), confirming its high ORR selectivity with 4 e^- transfer pathway. In addition**,** DA-FeNC exhibits the lowest Tafel slope of 46.8 mV dec^{-1} (**Figure 4c**), indicating faster reaction kinetics than NC, SA-FeNC, and commercial Pt/C. It should be noted that DA-FeNC achieves an outstanding kinetic current density (j_k) of 1.55 mA cm^{-2} at 0.85 V νs. RHE, as shown in **Figure 4d,** which is significantly higher than that of NC (0.03 mA cm^{-2}) and SA-FeNC (0.60 mA cm^{-2}), indicating the most rapid ORR kinetics on DA-FeNC. Furthermore, the mass-normalized site density (SD_{mass}) of the catalyst was determined by electrochemical nitrite (NO_2^-) adsorption and stripping in a 0.5 M acetate buffer solution (pH 5.2) [51, 52]. As depicted in **Figure S13-14**, the excess coulombic charge (Q_{strip}) associated with the stripping of DA-FeNC and SA-FeNC is 20.38 C g^{-1} and 16.32 C g^{-1}, respectively (**Table S6)**. The corresponding SD_{mass} for DA-FeNC and SA-FeNC were determined to be 2.54×10^{19} sites g^{-1} and 2.04×10^{19} sites g^{-1}, respectively (**Figure 4e**). Importantly, to further quantify the inherent activity of the catalysts, the average turnover frequencies (TOF) of their active sites were calculated. The TOF of DA-FeNC is 4.62 e $site^{-1}\ s^{-1}$, significantly higher than that of SA-FeNC (2.92 e $site^{-1}\ s^{-1}$), demonstrating that DA-FeNC exhibits the optimum intrinsic ORR activity. In addition, **Figure 4f** shows the durability comparison after 50,000 cycles. The $E_{1/2}$ of DA-FeNC displays a slight decay of approximately 26 mV, while the limiting current remains nearly constant. In contrast, Pt/C and SA-FeNC have a more $E_{1/2}$ loss of 52 mV and 45 mV, respectively (**Figure S15**). The lowest $E_{1/2}$ loss for DA-FeNC demonstrates its excellent cycling durability. Furthermore, the Raman spectra of DA-FeNC show no significant changes in both the D band and G band before and after the durability test (**Figure 4g**), further confirming its structural durability. Moreover, The ICP-MS after 50,000 cycles shows that the Fe concentration in the electrolyte is 19.05 μg L^{-1} for SA-FeNC, corresponding to a leaching ratio of 25.3%, whereas for DA-FeNC it is significantly lower at 9.77 μg L^{-1}, with a leaching ratio of only 6.67% (**Table S7**). This comparison clearly demonstrates that the dual-Fe sites DA-FeNC catalyst exhibits significantly suppressed Fe dissolution compared to the single-Fe sites SA-FeNC catalyst. The improved stability can be attributed to enhanced metal-support interactions and the synergistic stabilization effect of the dual-Fe sites configuration, which effectively inhibits Fe leaching under

acidic conditions. To further clarify the key role of Fe sites in DA-FeNC, a poisonous test with SCN^- ion was conducted by virtue of its strong affinity to Fe-N_x sites and thus inhibits their activity for ORR [53]. After the addition of KSCN (**Figure S16**), the E_{onset} and $E_{1/2}$ of DA-FeNC decrease from 0.92 V to 0.87 V and from 0.82 V to 0.76 V, respectively, confirming that the Fe centers are the primary active sites. Moreover, chronoamperometric (i-t)

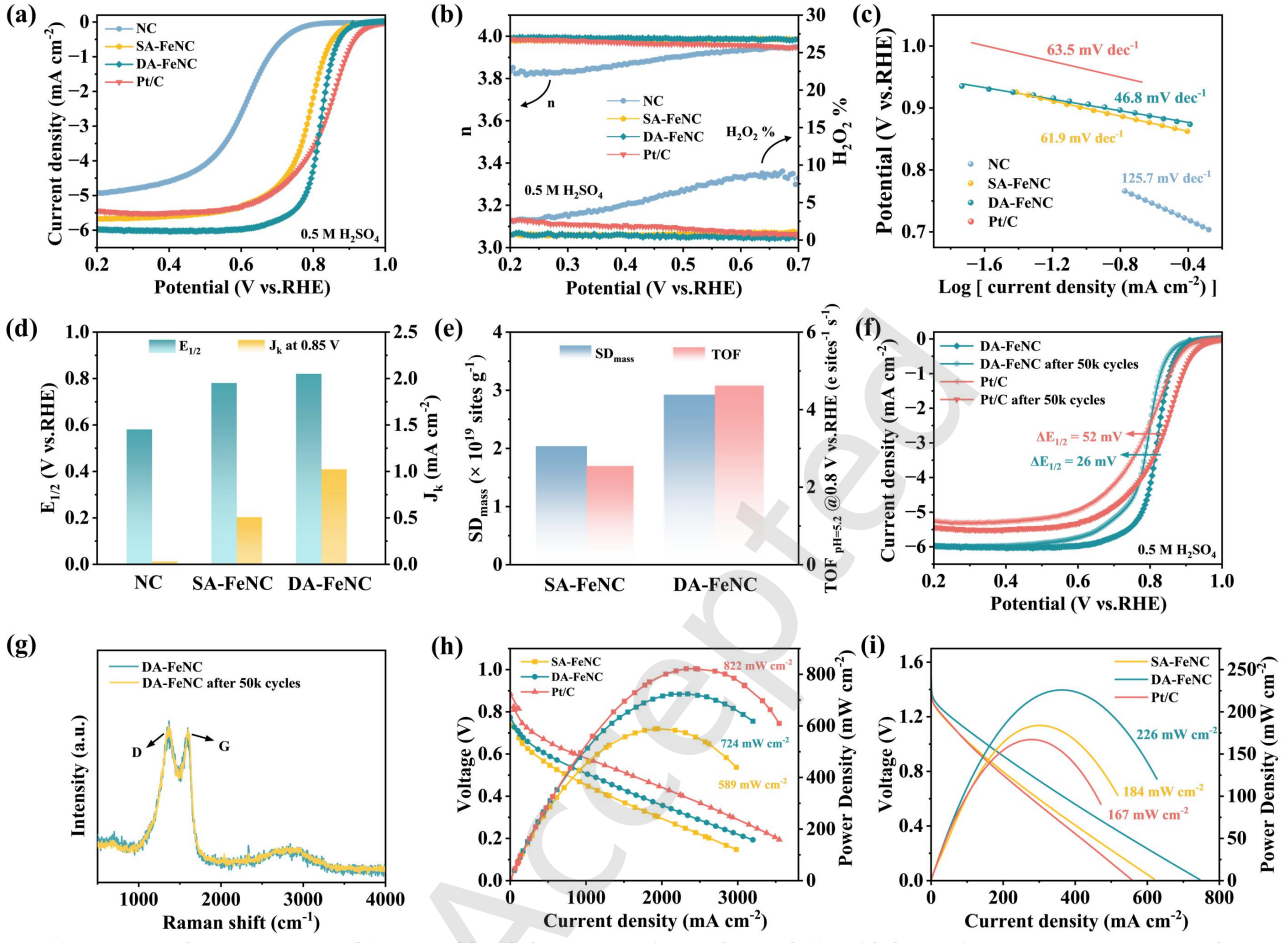

Figure 4 (a) ORR LSV polarization curves, (b) H_2O_2 yield and electron transfer number, and (c) Tafel slopes of NC, SA-FeNC, DA-FeNC, and commercial Pt/C in 0.5 M H_2SO_4; (d) Histograms of Half-wave potential ($E_{1/2}$) and kinetic current density (j_k) of NC, SA-FeNC, and DA-FeNC; (e) The mass-normalized site density (SD_{mass}) and turnover frequencies (TOF) of SA-FeNC and DA-FeNC for ORR; (f) Cycling durability comparison of DA-FeNC and Pt/C in 0.5 M H_2SO_4; (g) Raman spectra of DA-FeNC before and after 50,000 cycles in H_2SO_4; I-V polarization curves and power density plots of (h) PEMFC and (i) Zn-air batteries using SA-FeNC, DA-FeNC and Pt/C as cathode catalysts.

measurements were performed in 0.5 M H_2SO_4 electrolyte (150 mL) with the addition of 0.4 mL 3.0 M methanol to evaluate the methanol tolerance of the catalyst. As shown in the **Figure S17**, the current response of the DA-FeNC catalyst shows negligible change after methanol injection. In contrast, the commercial Pt/C catalyst exhibits rapid current drop, which is attributed to the fact that it is poisoned by methanol. These results demonstrate that DA-FeNC exhibits superior methanol tolerance and higher selectivity for the ORR compared to commercial Pt/C. Additionally, the ORR performance of DA-FeNC and SA-FeNC was assessed in O_2-saturated 0.1 M KOH. As shown in **Figure S18a**, DA-FeNC delivers the highest half-wave potential ($E_{1/2}$ = 0.93 V vs. RHE), which is superior to those of NC (0.81 V vs. RHE), SA-FeNC (0.89 V vs. RHE), and commercial Pt/C (0.86 V vs. RHE). Meanwhile, **Figure S18b** reveals that the H_2O_2 yield of DA-FeNC is less than 5.0%, and the corresponding n ranges from 3.90 to 3.99, confirming its dominant four-electron ORR pathway. Furthermore, the Tafel slope of DA-FeNC (55.8 mV dec^{-1}) is lower than that of the NC, SA-FeNC, and commercial Pt/C (**Figure S18c**), further indicating more favorable ORR kinetics on DA-FeNC. Correspondingly, **Figure S18d** shows the durability of DA-FeNC in 0.1 M KOH. DA-FeNC also exhibits exceptional durability, showing only a negligible 10 mV loss in $E_{1/2}$ after 50,000 cycles, even significantly outperforming Pt/C (41 mV loss). In comparison, SA-FeNC undergoes 28 mV decay (**Figure S19**). The above results confirm the critical role of the dual-Fe atom sites in enhancing ORR performance in both acid and alkaline media.

To further verify the ORR performance of DA-FeNC under practical conditions, single PEMFC and Zn-air battery tests were performed. **Figure 4h** presents the I-V polarization and power density curves of PEMFCs with DA-FeNC, SA-FeNC, and commercial Pt/C as cathodes. The DA-FeNC delivers a peak power density of 724 mW cm^{-2}, which achieves 88.08% of commercial Pt/C (0.05 mg_{Pt} cm^{-2}) and surpasses that of SA-FeNC (589 mW cm^{-2}). This enhanced performance is consistent with the ORR activity trends (**Figure 4a**). After 500 cycles, the peak power density for DA-FeNC is decreased by only 23.7% from 724 to 552 mW cm^{-2} (**Figure S20a**), while the SA-FeNC suffered from a rapid 25.6% loss with only a 100-cycle test (**Figure S20b**). Such

remarkable durability highlights the structural robustness of the dual-Fe atom sites and underscores their great promise for long-term operation under harsh acidic conditions. In addition, the Zn-air battery performance in **Figure 4i** shows that the highest power density achieved by DA-FeNC is 226 mW cm^{-2}, which is much higher than that of SA-FeNC (179 mW cm^{-2}) and commercial Pt/C (167 mW cm^{-2}). It should be noted that the catalyst loading in the test is the same for all samples. Moreover, the

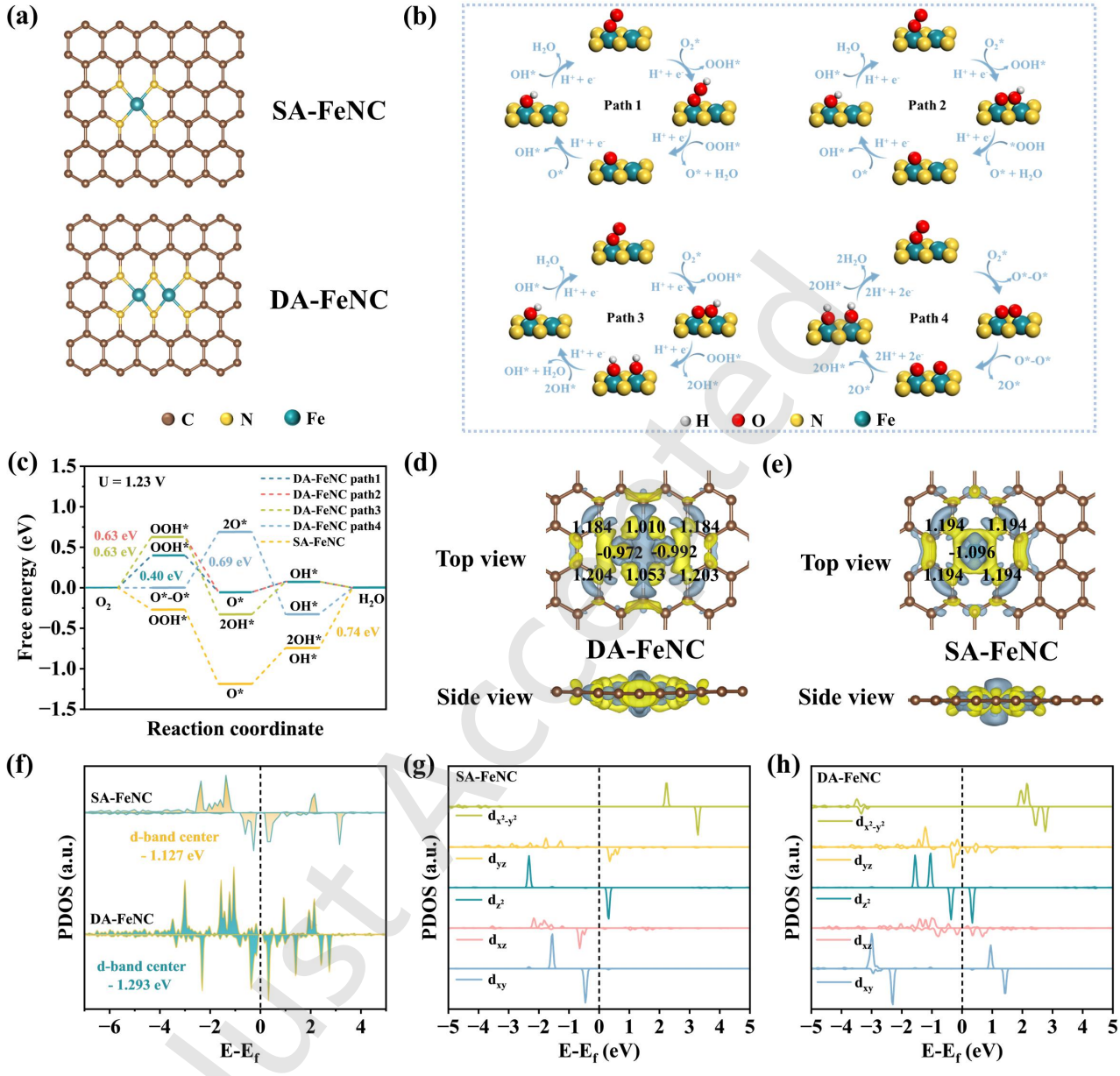

Figure 5 (a) Models for SA-FeNC and DA-FeNC; (b) Four possible ORR pathways on the DA-FeNC model; (c) ORR Free energy diagrams of DA-FeNC (four possible ORR pathways) and SA-FeNC at U = 1.23 eV; Charge densities and Bader charges of (d) DA-FeNC and (e) SA-FeNC, where blue and yellow indicate charge depletion and accumulation, respectively; (f) Partial density of states (PDOS) and d-band center positions of DA-FeNC and SA-FeNC (The Fermi level (E_f = 0 eV) is marked with a dotted line; PDOS for Fe 3d in different orientation (g) SA-FeNC and (h) DA-FeNC.

specific capacity of DA-FeNC at 10 mA cm^{-2}, as shown in **Figure S21**, reaches 815 mA h g^{-1}, surpassing that of commercial Pt/C (747 mA h g^{-1}). These full-cell testing results definitely confirm the great potential of DA-FeNC as a high-performance ORR catalyst in both PEMFCs and Zn-air batteries.

3.3 Theoretical calculations

The theoretical calculations based on DFT were carried out to elucidate the intrinsic catalytic mechanism of DA-FeNC for enhancing ORR performance. **Figure 5a** shows two structural models with FeN_4 and Fe_2N_6 sites constructed based on the characterized results from AC-HAADF-STEM observation (**Figure 2g-l**), XPS (**Figure 3b**), and EXAFS analyses (**Figure 3d**), representing SA-FeNC and DA-FeNC developed in the work, respectively. As for the calculation of ORR on DA-FeNC, a specific emphasis was placed on exploring distinct reaction pathways on DA-FeNC due to the fact that it has two Fe sites as active sites to adsorb O_2 and OOH* species, with monodentate and bridge configurations [28]. Moreover, the ORR process can proceed via either an associative or a dissociative pathway [54]. Therefore, four possible ORR pathways on DA-FeNC were considered. As shown in **Figure 5b**, in path 1, O_2 and all intermediates are adsorbed on a single Fe site, while in path 2, OOH* adsorbs

on Fe-Fe bridge bonds, whereas OH* and O* are adsorbed on a single Fe site. In path 3, OOH* adsorbs on Fe-Fe bridge bonds and subsequently dissociates into two OH* that are individually anchored on two Fe sites. In path 4, O_2 adsorbs on Fe-Fe bridge bonds, followed by the cleavage of the O-O bond into two O* species, thereby circumventing the formation of OOH*. The Gibbs free energy (ΔG) for each elementary step was calculated to evaluate the thermodynamics of the ORR process. Based on these calculations, the limiting reaction barrier, which critically determines catalytic performance, was derived from the free energy of the rate-determining step (RDS). As shown in **Figure S22,** all ORR steps on the DA-FeNC along the four pathways exhibit a downhill trend at U = 0 V, suggesting that these processes are thermodynamically favorable and proceed spontaneously under standard conditions. **Figure 5c** further shows the Gibbs free energy profiles at U = 1.23 V, in which the rate-determining step (RDS) in the four pathways occurs during the first electron-transfer step from O_2 to OOH*, and ΔG_{RDS} is 0.40, 0.63, 0.63, and 0.69 eV for path 1, path 2, path 3, and path 4, respectively. Among these, path 1 shows the lowest activation barrier, identifying it as the most favorable pathway for the ORR on DA-FeNC. For comparison, the ORR process on the SA-FeNC structure with path 1 was also calculated (**Figure S23**). As shown in **Figure 5c**, the RDS for SA-FeNC occurs in the final electron-transfer process from OH* to H_2O with a corresponding ΔG_{RDS} of 0.74 eV at U = 1.23 V, which is significantly higher than those of DA-FeNC in all four ORR paths. The results theoretically demonstrate the better ORR kinetics of DA-FeNC than those of SA-FeNC.

To elucidate the underlying mechanism of the dual-Fe sites in promoting ORR activity, both charge density differences and Bader charges on the DA-FeNC and SA-FeNC models were first calculated. As shown in **Figure 5d-e**, the charge density differences indicate that the dual Fe atoms in DA-FeNC have more charge density than the single Fe atom in SA-FeNC. Concretely, Bader charge analysis revealed that the two Fe atoms in DA-FeNC lost 0.972 e and 0.992 e, respectively, whereas the single Fe atom in SA-FeNC lost 1.096 e, indicating that the introduction of the secondary Fe site modifies the electronic distribution of the active centers. Moreover, to further understand the electronic modulation induced by the dual-Fe sites, the projected density of states (PDOS) of Fe 3d orbitals in DA-FeNC and SA-FeNC were calculated. As shown in **Figure 5f**, the Fe 3d electronic states of DA-FeNC are significantly broadened and more delocalized compared with those of SA-FeNC, indicating a higher degree of d-electron delocalization and enhanced orbital hybridization. Meanwhile, the d-band center of DA-FeNC is -1.293 eV, which is farther away from the Fermi level than that of SA-FeNC (-1.127 eV), implying a weakened adsorption strength toward key reaction intermediates. To further elucidate the nature of the above electronic structure evolution, the 3d orbital-resolved electronic states of individual Fe atoms were analyzed. As shown in **Figure 5g-h**, compared with SA-FeNC, the d_{yz}, d_{z^2}, and d_{xz} orbitals in DA-FeNC shift closer to the Fermi level, whereas the electronic states of the $d_{x^2-y^2}$ and d_{xy} orbitals collectively move toward lower energies. Further electron occupation analysis (**Table S8**) reveals that the average d-electron count of the Fe atom in DA-FeNC increases to 6.46, which is higher than that of SA-FeNC (6.32). Notably, the electron occupancy of the high-energy e_g orbitals (d_{z^2} and $d_{x^2-y^2}$) increases from 1.83 to 2.29, while that of the low-energy t_{2g} orbitals (d_{xy}, d_{xz}, and d_{yz}) markedly decreases from 4.49 to 4.17, clearly demonstrating an electron redistribution from the lower-energy t_{2g} orbitals to the high-energy e_g orbitals. These results indicate pronounced d-d orbital coupling between adjacent Fe sites in DA-FeNC, which induces d-band broadening and a downward shift of the d-band center, thereby facilitating optimized interactions with oxygen reaction intermediates.

Additionally, various metal sites usually follow a linear scaling relationship, with the free energy difference between OOH* and OH* ($\Delta G_{OOH^*} - \Delta G_{OH^*}$) remaining around 3.2 eV [55, 56]. In contrast, DA-FeNC exhibits a distinct deviation from this trend with a value of 2.78 eV), which can be attributed to the synergistic electronic interaction between the dual-Fe sites that modulates the adsorption of OOH* and OH*, thereby breaking the conventional scaling relation. This breakdown of the scaling relation suggests an intrinsic ability of DA-FeNC to balance the adsorption energies of key intermediates. To further substantiate this finding, the adsorption characteristics of OH were analyzed in detail. As shown in **Figure 6a**, the calculated OH* adsorption energy on DA-FeNC (-1.89 eV) is 0.60 eV higher than that on SA-FeNC (-2.69 eV), indicating weaker OH* binding. Furthermore, the Fe-O bond length in DA-FeNC (1.890 Å) is longer than that in SA-FeNC (1.821 Å), consistent with the weaker binding and suggesting more facile desorption. To reveal the underlying mechanism at the electronic-structure level, charge density difference and Bader charge analyses were performed for DA-FeNC and SA-FeNC after OH* adsorption. As shown in **Figure 6b**, less charge is transferred from DA-FeNC to OH* (0.431 e) than from SA-FeNC (0.504 e), further confirming its weaker interaction with OH*, in agreement with the adsorption energy results. In addition, the PDOS of DA-FeNC and SA-FeNC after OH* adsorption (**Figure 6c**) reveals a pronounced overlap between the Fe $3d_{z^2}$ and O $2p_z$ orbitals near the Fermi level, indicative of strong orbital hybridization and the formation of hybridized states with relatively weak energy-level splitting. Notably, DA-FeNC exhibits a higher density of Fe-O related states near the Fermi level, suggesting greater occupation of antibonding (σ*) states, which enhances the antibonding character and consequently reduces the OH* adsorption strength. Moreover, the crystal orbital Hamilton population (COHP) analysis was conducted to further elucidate the interaction between the Fe and OH*. As shown in **Figure S24** and **Table S9**, the total integrated crystal orbital Hamiltonian population (ICOHP) values for the Fe-O bond in DA-FeNC (-2.127 eV) are less negative than those in SA-FeNC (-2.924 eV), indicating a weaker Fe-O interaction in DA-FeNC after OH* adsorption. This observation is consistent with the Bader charge analysis, confirming the reduced electron transfer from Fe to OH* in DA-FeNC. To further reveal the orbital origin of the weakened Fe-O interaction, the COHP contributions between Fe 3d orbitals (d_{xy}, d_{yz}, d_{z^2}, d_{xz}, and $d_{x^2-y^2}$) and O 2p orbitals (p_x, p_y, and p_z) were decomposed. The corresponding ICOHP values (**Table**

S9) demonstrate that the Fe-OH* bonding interaction is predominantly governed by the coupling between Fe $3d_z^2$ and O $2p_z$ orbitals, which forms a characteristic head-on σ/σ* bonding interaction. This finding highlights the dominant role of $3d_z^2$-$2p_z$ orbital overlap in the formation of the Fe-O bond. Specifically, the ICOHP values for the $3d_z^2$-$2p_z$ interaction are -0.729 eV for DA-FeNC and -1.156 eV for SA-FeNC. Further COHP analysis (**Figure 6d**) clearly resolves the electronic coupling characteristics between the $3d_z^2$ and $2p_z$orbitals. Compared with SA-FeNC, DA-FeNC shows a pronounced increase in the occupation of σ* antibonding states derived

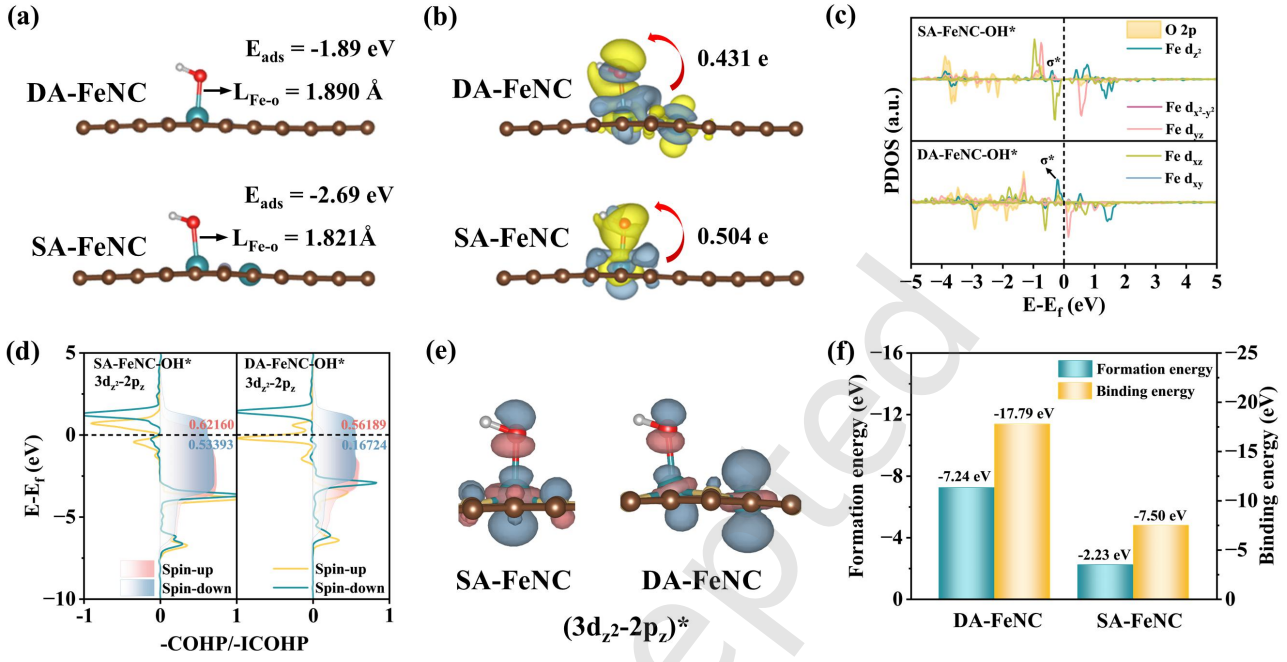

Figure 6 (a) Adsorption energies of OH* and the corresponding Fe-O bond lengths on DA-FeNC and SA-FeNC; (b) Charge density distributions and Bader charge diagrams of DA-FeNC and SA-FeNC after OH* adsorption; (c) PDOS for Fe 3d in different orientation SA-FeNC and DA-FeNC after OH* adsorption; (d) Projected crystal orbital Hamilton population (COHP) between the active metal center Fe $3d_z^2$ and O $2p_z$ in SA-FeNC and DA-FeNC after OH* adsorption; (e) Visualization of the $(3d_z^2$-$2p_z)$* orbital shapes for SA-FeNC and DA-FeNC after OH* adsorption; (f) Formation energies and binding energies between Fe and N of DA-FeNC and SA-FeNC.

from the $(3d_z^2$-$2p_z)$* interaction, thereby weakening the Fe-O bond (**Figure 6e**). These orbital-level insights provide compelling electronic-structure evidence for the intrinsically reduced OH* adsorption in DA-FeNC. In addition, the formation energy (E_f) and binding energy (E_b) of dual-Fe and single-Fe sites anchoring in the N-doped carbon substrate were further calculated. As shown in **Figure 6f**, DA-FeNC exhibits a E_f of -7.24 eV and an E_b of -17.79 eV, both of which are significantly more negative than those of SA-FeNC (-2.23 eV and -7.50 eV, respectively), indicating that the dual-Fe sites are thermodynamically more stable and more strongly anchored on the N-doped carbon substrate, which is beneficial for enhancing the structural stability and long-term durability of the catalyst.

Through theoretical study, the cooperative electronic coupling between adjacent Fe sites in DA-FeNC can effectively reconstruct the local electronic structure of the Fe active centers, leading to an increase in the electron occupancy of the Fe 3d e_g orbitals and a decrease in the occupancy of the t_{2g} orbitals, and a broadening accompanied by a downshift of the d-band center relative to the Fermi level, thereby rationally tuning the adsorption strength of oxygen intermediates. Notably, the dual Fe sites synergistically regulate the interaction between Fe $3d_z^2$ and O $2p_z$ orbitals, enhancing the occupation of σ* antibonding states, thereby effectively weakening the adsorption of OH* on DA-FeNC. Effective modulation of OH* adsorption enables DA-FeNC to significantly deviate from the conventional OOH*/OH* linear scaling relationship, thereby introducing additional degrees of freedom for further lowering reaction energy barriers. Consequently, the RDS shifts from the final OH* desorption to the initial OOH* formation, while the overall reduction in the key reaction barriers makes the ORR process more favorable both thermodynamically and kinetically, ultimately resulting in a lower overpotential, accelerated reaction kinetics, and a reduced Tafel slope, consistent with the experimental observations. Meanwhile, the dual Fe sites exhibit stronger anchoring effects on the nitrogen-doped carbon substrate and higher thermodynamic stability, thereby significantly improving the structural stability and long-term durability of the catalyst. In summary, the synergistic integration of electronic structure modulation, optimized reaction kinetics, and enhanced structural stability endows DA-FeNC with a lower ORR overpotential and superior overall catalytic performance, highlighting the substantial potential of diatomic site configurations in the design of highly efficient ORR catalysts.

On the other hand, **Table S10-S11** summarizes the reported strategies of synthesizing dual-atom FeNCs. Among them, the host-guest encapsulation strategy has been widely applied, in which metal-organic frameworks (MOFs) serve as hosts to confine metal precursors within their ordered porous structures via impregnation, followed by high-temperature pyrolysis to construct dual-atom sites [26, 27]. Owing to their high surface area, tunable pore structures, and abundant coordination sites, MOFs can confine metal

precursors during thermal treatment while simultaneously serving as carbon/nitrogen sources to generate porous N-doped carbon frameworks that provide coordination environments and electronic coupling interfaces for dual-atom sites upon pyrolysis. However, this strategy strongly dependence on precise control of metal loading, making it difficult to achieve structurally well-defined and uniformly distributed dual-atom configurations. By contrast, loading metal dimer precursors onto N- and C-rich supports pre-defines the dual-metal configuration at the molecular level [28-30]. This approach takes advantage of the intrinsic metal–metal distance and coordination environment within the molecular precursor, enabling structural inheritance during pyrolysis through ligand carbonization, thereby suppressing random migration of metal atoms and their aggregation into nanoparticles and preserving the structural integrity of dual-metal sites. Nevertheless, the scarcity and limited stability of such dimers restrict compositional diversity and broader applicability. Another important approach is the defect engineering, which involves precisely engineering defect-rich structures around the FeN_x centers of FeNCs to serve as anchoring sites for secondary metal atoms, thereby forming dual-atom configurations [31,32]. While this strategy offers greater flexibility in catalyst design, it remains challenging to precisely regulate the type, density, and spatial distribution of defects, which critically influence the coordination environment and catalytic performance. These strategies have markedly advanced the development of dual-atom MNCs. However, they predominantly rely on anchoring metal ions or FeN_x moieties onto N-doped carbon supports, which in turn lead to structural instability and poor durability under operating conditions, especially in harsh acidic media. In contrast, our novel precursor design strategy employs a Fe-ion coordination polymer with a binuclear ligand synthesized from TCPP and DAP, in which the macrocyclic cavity and amide groups act as primary and secondary complexation sites, respectively. During thermal treatment, the metal coordination centers and the NC framework undergo synergistic carbonization, achieving tight coupling between the dual-Fe active sites and the carbon skeleton. This process significantly enhances the interaction between the metal centers and the carbon substrate, effectively suppresses metal atom migration and aggregation, and ensures a highly uniform distribution and structural integrity of the dual-atom sites. As a result, the obtained DA-FeNC catalyst exhibits superior catalytic performance and durability, particularly in a harsh acid medium. **Table S10** lists the comparison of the DA-FeNC developed in the work and other advanced Fe-based catalysts for ORR in an acidic medium. The DA-FeNC exhibits an $E_{1/2}$ of 0.82 V, with only 26 mV decay after 50k cycles. Meanwhile, the $E_{1/2}$ further increases to 0.93 V, with the cycling-induced decay significantly reduced to 10 mV in alkaline media (**Table S11**). The comprehensive comparison reveals that the DA-FeNC catalyst simultaneously achieves high catalytic activity and excellent long-term stability across different reaction environments, outperforming most of the reported dual-atom and single-atom Fe-based ORR catalysts. These results demonstrate that the binuclear ligand polymer designed at a molecular level is an effective strategy to construct highly active and long-term stable MNCs with dual metal atoms for ORR.

4 Conclusion

A FeNC with dual-Fe atom sites exhibiting excellent ORR performance in both acidic and alkaline media was precisely fabricated by pyrolyzing a newly designed binuclear ligand polymer synthesized from TCPP and DAP via a condensation reaction. In the precursor, the porphyrin in TCPP and the amide groups generated from the condensation combined with the pyridine in DAP serve as the primary and secondary coordination sites for Fe ion. Benefiting from this molecular-level binuclear ligand precursor design, dual-Fe sites are precisely synthesized and stably anchored within the FeNC, while simultaneously generating a hierarchical porous structure favorable for efficient mass transport. Meanwhile, compared with FeNC with single-Fe sites, the dual-Fe sites exhibit a pronounced cooperative electronic coupling effect with an increased Fe 3d orbital occupancy, which downshifts the d-band center and enhances the population of σ* antibonding states between Fe $3d_{z^2}$ and O $2p_z$ orbitals, thereby effectively optimizing the adsorption behavior of OH*. Such modulation of key intermediate adsorption breaks the conventional $\Delta G = OOH^*-OH^*$ scaling relationship of single-Fe atom sites and shifts the rate-determining step from OH* desorption to OOH* formation, with a reduced energy barrier of only 0.40 eV, thereby accelerating the reaction kinetics. Attributed to these structural and electronic advantages, the FeNC with Fe-Fe distance of approximately 2.7 Å delivers $E_{1/2}$ of 0.82 V and 0.93 V (vs. RHE) in acidic and alkaline media, respectively, with minimal potential losses of 26 mV and 10 mV after 50,000 cycles, outperforming most of reported dual-atom FeNCs synthesized by other strategies. Moreover, as a cathode catalyst in PEMFCs and Zn-air batteries, it achieves high peak power densities of 724 mW cm^{-2} and 226 mW cm^{-2}, respectively. In summary, the strategy of constructing dual-atom MNCs based on the new precursor of binuclear ligand amide polymer developed in the work provides an effective route for developing dual-atom MNCs with advanced ORR performance. Additionally, it is expected that this binuclear precursor can be readily extended to synthesize a wide variety of homo and heteronuclear dual-atom MNCs for the development of next-generation non-precious metal catalysts for sustainable energy conversion.

Electronic Supplementary Material: Supplementary material (please provide the brief detail of the ESM) is available in the online version of this article at https://doi.org/10.26599/NR.2026.94908848.

Data availability

All data needed to support the conclusions in the paper are presented in the manuscript and/or the Electronic Supplementary Material. Additional data related to this paper may be requested from the corresponding author upon request.

Acknowledgements

This work was financially supported by the National Natural Science Foundation of China (22075055) and the Guangxi Science and Technology Project (AB16380030). The authors appreciated the Center for Instrumental Analysis of Guangxi

University for providing facilities and resources.

Declaration of competing interest

All the contributing authors report no conflict of interests in this work.

Author contribution statement

LiZhen Wen: Writing - original draft, methodology, investigation, formal analysis. Weiqi Liang: Methodology, investigation. Wanling Xiao: Methodology. Cunhuai Yua: Methodology. Jiawang Li: Investigation. Yunbo Li: Investigation. ChengFu Tan: Investigation. Lijuan Wu: Investigation. Pei Kang Shen: Resources. Zhi Qun Tian: Writing - review & editing, supervision, resources, funding acquisition, formal analysis, conceptualization. All the authors have approved the final manuscript.

Use of AI statement

None

References

[1] Lin, M.; Hao, C.; Yang, B.; Liu, J.; Tan, C.; Wang, Z.; Xie, Y.; Shen, P. K.; Tian, Z. Q., Ultra-low Pt loading cathode catalyst layers with hierarchically mesoporous distribution modulation for high-performance proton exchange membrane fuel cells. *Nano Res.* **2025**, *18* , 94907824.

[2] Lan, L. S.; Wu, Y. G.; Pei, Y. F.; Wei, Y. H.; Hu, T.; Lützenkirchen-Hecht, D.; Yuan, K.; Chen, Y. W. High‐density accessible iron single‐atom catalyst for durable and temperature‐adaptive laminated Zinc‐air batteries. *Adv. Mater.* **2025**, *37*, 2417711.

[3] Shen, D.; Sun, F. F.; Liang, Z. J.; Fu, H. G.; Wang, L. Axial‐N induced square‐pyramidal crystal filed of atomically iron sites for enhancing acidic oxygen reduction. *Angew. Chem., Int. Ed.* **2025**, 64, e202505937.

[4] Zhao, Y. G.; Adiyeri Saseendran, D. P.; Huang, C.; Triana, C. A.; Marks, W. R.; Chen, H.; Zhao, H. Patzke, G. R., Oxygen evolution/reduction reaction catalysts: From in situ monitoring and reaction mechanisms to rational design. *Chem. Rev.* **2023**, 123, 6257-6358.

[5] Yu, Y.; Wang, Y.; Yang, F.; Feng, D.; Yang, M. Y.; Xie, P. F.; Zhu, Y. Z.; Shao, M. H.; Mei, Y. Li, J. C. Meso/microporous single-atom catalysts with curved Fe-N_4 sites boost the oxygen reduction reaction activity. *Angew. Chem., Int. Ed.* **2024**, 64, e202415691.

[6] Bhuvanendran, N.; Ravichandran, S. Lee, S. Sanij, F. D.; Kandasamy, S.; Pandey, P.; Su, H.; Lee, S. Y. Recent progress in Pt-based electrocatalysts: A comprehensive review of supported and support-free systems for oxygen reduction. *Coord. Chem. Rev.* **2024**, 521, 216191.

[7] Li, Y.; Jiang, H.; Lin, L.; Sun, Z.; Sun, G., Single-atomic iron synergistic atom-cluster induce remote enhancement toward oxygen reduction reaction. *J. Energy Chem.* **2025**, 102, 413-420.

[8] Zhang, H. W.; Chen, H. C.; Feizpoor, S.; Li, L. f.; Zhang, X.; Xu, X. f.; Zhuang, Z. c.; Li, Z. s.; Hu, W. y.; Snyders, R.; Wang, D. s.; Wang, C. d., Tailoring oxygen reduction reaction kinetics of Fe-N-C catalyst via spin manipulation for efficient Zinc-air batteries. *Adv. Mater.* **2024**, 36, 2400523.

[9] Wu, G. Zelenay, P. Activity versus stability of atomically dispersed transition-metal electrocatalysts. *Nat. Rev. Mater. 2024*, 9, 643-656.

[10] Dong, L. D.; Yu, C. H.; Yan, B. W.; Li, J. W.; Yang, B.; Lin, M. J.; Huang, J.; Xiao, W. L.; Zhong, J. B.; Shen, P. K.; Tian, Z. Q. Atomic rare‐earth Gd‐N‐C nanosheets with low f‐d‐p hybridization energy for efficient oxygen reduction reaction. *Adv. Funct. Mater.* **2025**, 35, 2501884.

[11] Luo, E. G.; Chu, Y. Y.; Liu, J.; Shi, Z. P.; Zhu, S. Y.; Gong, L. Y.; Ge, J. J.; Choi, C. H.; Liu, C. P.; Xing, W. Pyrolyzed M-N_x catalysts for oxygen reduction reaction: progress and prospects. *Energ. Environ. Sci.* **2021**, 14, 2158-2185.

[12] Zhang, J. C.; Li, F. H.; Liu, W.; Wang, Q. L.; Li, X. N.; Hung, S. F.; Yang, H. B. Liu, B. Modulating spin of atomic manganese center for high-performance oxygen reduction reaction. *Angew. Chem., Int. Ed.* **2024**, 63, e202412245.

[13] Zhao, Y. S.; Wan, J. W.; Ling, C. Y.; Wang, Y. L.; He, H. Y.; Yang, N. L.; Wen, R.; Zhang, Q. H.; Gu, L.; Yang, B. L.; Xiang, Z. H.; Chen, C.; Wang, J. L.; Wang, X.; Wang, Y. C.; Tao, H. B.; Li, X. N.; Liu, B.; Zhang, S. J.; Wang, D. Acidic oxygen reduction by single-atom Fe catalysts on curved supports. *Nature*, **2025**, 644, 668-675.

[14] Sun, H.; Deng, Z.; Li, J.; Zhang, S.; Li, M.; Jin, H.; Zhao, Z. Low-porosity carbon templates mitigate mass transport limitations in Fe-N-C catalysts. *Nano Res.* **2026**, 19, 94908227.

[15] Wang, Z.; Deng, D.; Zhang, W.; Cheng, X.; Xu, L.; Qian, J.; Li, H. Tailoring Mn–N_4 electronic structure via sulfur coordination for superior oxygen reduction electrocatalyst in zinc-air batteries. *J. Energy Chem.* **2025,** *110*, 647-656.

[16] Wang, S.; Chu, Y. Y.; Lan, C.; Liu, C. P.; Ge, J. J.; Xing, W. Metal-nitrogen-carbon catalysts towards acidic ORR in PEMFC: fundamentals, durability challenges, and improvement strategies. *Chem. Synth.* **2023**, 3, 2101222.

[17] Yin, S. H.; Chen, L.; Yang, J.; Cheng, X. Y.; Zeng, H. B.; Hong, Y. H.; Huang, H.; Kuai, X. X.; Lin, Y. G.; Huang, R.; Jiang, Y. X.; Sun, S. G. A Fe-NC electrocatalyst boosted by trace bromide ions with high performance in proton exchange membrane fuel cells. *Nat. Commun.* **2024**, 15, 7489.

[18] Guan, G. J.; Liu, Y. H.; Li, F. H.; Shi, X. W.; Liu, L. Y.; Wang, T. Y.; Xu, X. T.; Zhao, M.; Ding, J.; Yang, H. B. Atomic cobalt metal centers with asymmetric N/B-coordination for promoting oxygen reduction reaction. *Adv. Funct. Mater.* **2024**, 34, 2408111.

[19] Bai, J. R.; Sun, Z. Z.; Zhang, H. Y.; Lian, Y. B.; Deng, Y. Y.; Xiang, M.; Su, Y. Q. Modulating the local coordination environment of M-N_x single-atom site for enhanced electrocatalytic oxygen reduction. *Adv. Funct. Mater.* **2024**, 35, 2417013.

[20] Li, J.; Sun, C.; Fan, H.; Dong, F.; Lv, Z.; Liu, R.; Yang, W.; Wang, B., Boosting active site accessibility and alleviating mass transfer resistance for high-performance fuel cells. *Nano Res.* **2025**, 18, 94907654.

[21] Zhang, Z.; Xing, Z. Y.; Luo, X. L.; Cheng, C.; Liu, X. K. Densely populated macrocyclic dicobalt sites in ladder polymers for low-overpotential oxygen reduction catalysis. *Nat. Commun.* **2025**, 16, 921.

[22] You, S. P.; Zhang, C.; Yu, M. Y.; Tan, X.; Sun, K. A.; Zheng, Y.; Zhuang, Z. W.; Yan, W.; Zhang, J. J. Rational dual‐atom design to boost oxygen reduction reaction on iron‐based electrocatalysts. *Small*, **2025**, 21, 2502102.

[23] Yuan, L. J.; Miao, Z. Y.; Sui, X. L.; Lee, C. F.; Li, Q.; Yin, M. J.; Shen, L. X.; Lu, Y. R.; Zhao, Z. G.; Liu, Y. Z.; Zhu, L. S.; Gong, W.; Feng, W. L.; Wang, H. T.; Zhang, G. X.; Wang, Z. B. Janus effect of FeCo dual atom catalyst with Co as active center in acidic oxygen reduction reaction. *Nat. Commun.* **2025**, 16, 7198.

[24] Zhang, W. Y.; Yi, S. Y.; Yu, Y. H.; Liu, H.; Kucernak, A.; Wu, J.; Li, S. Fe-based dual-atom catalysts for the oxygen reduction reaction. *J. Mater. Chem. A* **2024**, 12, 87-112.

[25] Wei, L.; Zhang, X.; Xu, Z.; Shu, X.; Lou, H.; Lan, F.; Gu, S.; Chen, G.; Zeng, Q.; Sui, M.; Ke, X., Hierarchically porous hollow architecture hosting dense Co/Fe single-atom sites for synergistic oxygen electrocatalysis. *J. Energy Chem.* **2026**, 116, 854-862.

[26] Liu, H. Q.; Huang, J. Z.; Feng, K.; Xiong, R.; Ma, S. Y.; Wang, R.; Fu, Q.; Rafique, M.; Liu, Z. G.; Han, J. C.; Hua, D. X.; Li, J. J.; Zhong, J.; Wang, X. J.; Zhao, Z. L.; Yao, T.; Jiang, S. D.; Xu, P.; Zhang, Z. H.; Song, B. Reconstructing the coordination environment of Fe/Co dual-atom sites towards efficient oxygen electrocatalysis for Zn-air batteries. *Angew. Chem., Int. Ed.* **2024**, 64, e202419595.

[27] Xiao, M. L.; Chen, Y. T.; Zhu, J. B.; Zhang, H.; Zhao, X.; Gao, L. Q.; Wang, X.; Zhao, J.; Ge, J. J.; Jiang, Z.; Chen, S. L.; Liu, C. P.; Xing, W. Climbing the apex of the ORR volcano plot via binuclear site construction: electronic and geometric engineering. *J. Am. Chem. Soc.* **2019**, 141, 17763-17770.

[28] Li, Y. Q.; Luo, X.; Wei, Z. H.; Zhang, F.; Sun, Z. Y.; Deng, Z. W.; Zhan, Z. H.; Zhao, C. F.; Sun, Q.; Zhang, L.; Chen, W. X.; Li, S. H.; Pang, S. P. Precisely constructing charge-asymmetric dual-atom Fe sites supported on hollow porous carbon spheres for efficient oxygen reduction. *Energ. Environ. Sci.* **2024**, 17, 4646-4657.

[29] Leng, K. Y.; Zhang, J. T.; Wang, Y.; Li, D. D.; Bai, L.; Shi, J. B.; Li, X. L.; Zheng, L. R.; Bai, J. B.; Qu, Y. T. Interfacial cladding engineering suppresses atomic thermal migration to fabricate well‐defined dual‐atom electrocatalysts. *Adv. Funct. Mater.* **2022**, 32, 2205637.

[30] Zeng, Y. Z.; Wang, X.; Qi, W.; Liu, C. P.; Lu, L. L.; Xiao, M. L.; Li, K.; Xiao, F.; Shao, M. H.; Xing, W.; Zhu, J. B. Aligned d-orbital energy level of dual-atom sites catalysts for oxygen reduction reaction in anion exchange membrane fuel cells. *Nat. Commun.* **2025**, 16, 8111.

[31] Tang, B.; Zhou, Y. N.; Ji, Q. Q.; Zhuang, Z. C.; Zhang, L.; Wang, C.; Hu, H. B.; Wang, H. J.; Mei, B. B.; Song, F.; Yang, S.; Weckhuysen, B. M.; Tan, H.; Wang, D. S.; Yan, W. S. A Janus dual-atom catalyst for electrocatalytic oxygen reduction and evolution. *Nat Synth.* **2024**, 3, 878-890.

[32] Zhao, S.; Liu, M. J.; Qu, Z. H.; Yan, Y.; Zhang, Z. R.; Yang, J. F.; He, S. Y.; Xu, Z.; Zhu, Y. Q.; Luo, L. H.; Hui, K. N.; Liu, M. K.; Zeng, J. Cascade synthesis of Fe - N_2 - Fe dual - atom catalysts for superior oxygen catalysis. *Angew. Chem., Int. Ed.* 2024, 63, e202408914.

[33] Kohn,W.; Sham, L. J. Self-consistent equations including exchange and correlation effects. *Phys. Rev.* **1965**, 140, A1133-A1138.

[34] Kresse, G.; Joubert, D. From ultrasoft pseudopotentials to the projector augmented-wave method. *Phys. Rev.* B **1998**, 59, 1758 -1775.

[35] Perdew, J. P.; Chevary, J. A.; Vosko, S. H.; Jackson, K. A.; Pederson, M. K.; Singh, D. J. Atoms, molecules, solids, and surfaces: Applications of the generalized gradient approximation for exchange and correlation. *Phys. Rev.* B **1992**, 46, 6671-6687.

[36] Grimme, S.; Ehrlich, S.; Goerigk, L. Effect of the damping function in dispersion corrected density functional theory. *J. Comput. Chem.* **2011**, 32, 1456-1465.

[37] Monkhorst, H. J.; Pack, J. D. Special points for Brillouin-zone integrations. *Phys. Rev.* B **1976**, 13, 5188-5192.

[38] Liu, B.; Li, J. W.; Yan, B. W.; Wei, Q.; Wen, X. Y.; Xie, H. R.; He, H.; Shen, P. K.; Tian, Z. Q. Sulfur doped iron-nitrogen-hard carbon nanosheets as efficient and robust noble metal-free catalysts for oxygen reduction reaction in PEMFC. *J. Energy. Chem.* **2024**, 89, 422-433.

[39] Zhu, D. Y.; Wu, H. W.; Fong, W. K.; Tabor, R. F.; Zhang, J. The ratio of sp^2 and sp^3 hybridized carbon determines the performance of carbon - based catalysts in H_2O_2 electrosynthesis from O_2. *Angew. Chem., Int. Ed.* **2025**, 64, e202500145.

[40] Zhu, Y. W.; Jiang, Y. M.; Li, H. J. W.; Zhang, D. C.; Tao, L.; Fu, X. Z.; Liu, M.; Wang, S. Y. Tip-like Fe-N_4 sites induced surface microenvironments regulation boosts the oxygen reduction reaction. *Angew. Chem., Int. Ed.* **2024**, 63, e202319370.

[41] Zeng, Y. Q.; Zhao, J.; Wang, S. F.; Wang, W. J.; Lu, Y. R.; Xi, S. B.; Xu, W.; Yoda, Y.; Masuda, R.; Li, X. N.; Huang, Y. Q.; Liu, B.; Zhang, T. Unraveling the dynamic low-spin state evolution of single-Fe-atom sites for efficient CO_2 electroreduction. *J. Am. Chem. Soc.* **2025**, 147, 42539-42548.

[42] Xu, X. Q.; Gan, T.; Guan, J. Q. Spin engineering of dual-atom Fe_2 catalysts for oxygen reduction. CCS Chem. **2025**, 8, 350-367.

[43] Yan, L.; Mao, Y.; Li, Y. X.; Sha, Q. H.; Sun, K.; Li, P. P.; Waterhouse, G. I. N.; Wang, Z. Y.; Tian, S. B.; Sun, X. M. Sublimation transformation synthesis of dual - atom Fe catalysts for efficient oxygen reduction reaction. *J. Am. Chem. Soc.* **2024**, 64, e202413179.

[44] Zhang, H.; Jiang, J. J.; Li, B. J.; Yang, C. Y.; Bo, S. W.; An, Q. Z.; Liu, Q. H.; He, S.; Zhou, W. L Precisely regulating the electronic configuration of Fe-N_4 units for practical oxygen reduction reactions. *Chem. Eng. J.* **2025**, 506, 159888.

[45] Chen, T.; Hao, C.; Chen, Z. Y.; Li, J. W.; Lin, C. Q.; Shen, P. K.; Tian, Z. Q. Exposure engineering of active sites of Co-N-C for efficient oxygen reduction reaction . *Chem. Eng. J.* **2025**, 505, 159449.

[46] Jiang, P.; Li, P.; Yang, Y.; Chen, C.; Ye, C.; Zhang, L.; Hu, H.; Zhang, Y.; Zhou, H.; Gao, X.; Zhao, Y.; Su, C.; Wu, Y., Symbiotic topological defect with atomic Fe sites for enhanced electrocatalytic oxygen reduction. *Nano Res.* **2024**, 18, 94907532.

[47] Zhao, C.; Chu, B. X.; Nian, H.; Shao, B.; Lu, Y.; Zhang, F. C.; Wang, Y. G.; Xu, Q. Sulfur - mediated microenvironment modulation of high - density Fe - N_4 sites for high - efficiency oxygen reduction and cryotolerant quasi - solid - state Zinc - air batteries. *Adv. Mater.* **2025**, 37, e10621.

[48] Li, N.; Li, M. Y.; Guo, K.; Guo, Z. Q.; Wang, R. J.; Bao, L. P.; Hou, G. L.; Lu, X. Deciphering the role of native defects in dopant - mediated defect engineering of carbon electrocatalysts. *Adv. Energy Mater*. **2024**, 14, 2401008.

[49] Du, J.; Liu, Y. C.; Sun, M.; Guan, J.; Chen, A. B.; Han, B. X. Highly selective oxygen electroreduction to hydrogen peroxide on sulfur - doped mesoporous carbon. *Angew. Chem., Int. Ed.* **2025**, 64, e202503385.

[50] Zheng, S.; Fu, Y. B.; Xu, X. Y.; Xu, Q.; Zeng, G. F. Integrating electronic - storage piperazine into covalent organic frameworks for promoting oxygen reduction reaction. *Angew. Chem., Int. Ed.* **2025**, 64, e202503434.

[51] Li, J. W.; Lin, C. Q.; Chen, Z. Y.; Huang, J.; Yang, B.; Lin, M. J.; Shen, P. K.; Tian, Z. Q. Fe–N–C electrocatalyst with d-π interaction induced by submicropore vacancies for durable oxygen reduction reaction in proton-exchange membrane fuel cells. *ACS Catal.* **2025**, 15, 20512-20530.

[52] Malko, D.; Kucernak, A.; Lopes, T. T Lopes. In situ electrochemical quantification of active sites in Fe–N/C non-precious metal catalysts. *Nat. Commun.* **2016**, 7, 13285.

[53] Zhao, Y. L.; Chen, H. C.; Ma, X. L.; Li, J. Y.; Yuan, Q.; Zhang, P.; Wang, M. M.; Li, J. X.; Li, M.; Wang, S. F.; Guo, H.; Hu, R. B.; Tu, K. H.; Zhu, W.; Li, X. N.; Yang, X.; Pan, Y. Vacancy defects inductive effect of asymmetrically coordinated single - atom Fe-N_3S_1 active sites for robust electrocatalytic oxygen reduction with high turnover frequency and mass activity. *Adv. Mater.* **2023**, 36, 2308243.

[54] L Q Liu, J Y Hu, X B Rao, et al. Revealing the dependence of oxygen reduction mechanism and activity on the D-band center difference of Fe-M bimetallic sites [J]. *Appl. Catal. B:Environ. Energy* **2026**, 384, 126191.

[55] Lee, D. G.; Kim, S. H.; Lee, H. H.; Shin, S.; Lee, J.; Joo, S. H.; Lee, Y.; Kwak, S. K.; Song, H. K. Breaking the linear scaling relationship by a proton donor for improving electrocatalytic oxygen reduction kinetics. *ACS Catal.* **2021**, 11, 12712-12720.

[56] Xia, H. Y.; Sun, M. Z.; Yang, D. Y.; Pang, D. Y.; Zeng, D. Y.; Huang, L.; Huang, B. L.; Li, B.; Wang, E. R. Phosphorus/sulfur-modulated p-band center of pentagonal carbon for efficient oxygen reduction reaction. *J. Am. Chem. Soc.* **2025**, 147, 41472-41480.

Electronic Supplementary Material

Iron coordinated by nitrogen doped carbon with dual-iron atom sites derived from binuclear ligand polymer for efficient oxygen reduction reaction

LiZhen Wen[1,2,3], Weiqi Liang[1,2,3], Wanling Xiao[1,2,3], Cunhuai Yu[1,2,3], Jiawang Li[1,2,3], Yunbo Li[1,2,3], ChengFu Tan[1,2,3], Lijuan Wu[1,2,3], Pei Kang Shen[1,2,3], and Zhi Qun Tian [1,2,3]

[1] *Collaborative Innovation Center of Sustainable Energy Materials, School of Physical Science and Technology, Guangxi University; Nanning 530004, China*
[2] *Guangxi Key Laboratory of Electrochemical Energy Materials, Nanning 530004, China*
[3] *State Key Laboratory of Featured Metal Materials and Life-cycle Safety for Composite Structures, Nanning 530004, China*

Supporting information to https://doi.org/10.26599/NR.2026.94908848

Address correspondence to tianzhiqun@gxu.edu.cn

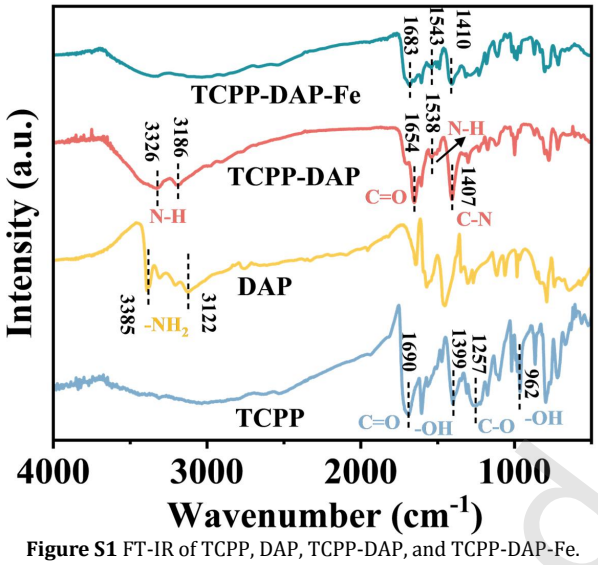

Figure S1 FT-IR of TCPP, DAP, TCPP-DAP, and TCPP-DAP-Fe.

For TCPP, the vibration bands of C=O in carboxyl group at ~1690 cm^{-1}, the broad absorption band corresponding to the C-O stretching at ~1257 cm^{-1}, and the bending vibration of -OH in carboxyl group are observed at ~1399 cm^{-1} and ~962 cm^{-1}. For DAP, the absorption bands at 3300 cm^{-1} -3450 cm^{-1} are consistent with the stretching of the NH_2 group. After TCPP and DAP reactions, the vibration peaks of C-O and -OH in TCPP disappeared, and the -NH_2 vibration peaks in DAP changed. Concurrently, new prominent bands appeared at ~1538 cm^{-1} and ~1654 cm^{-1} in TCPP-DAP, corresponding to -NH- bending and C=O stretching vibrations, respectively, indicating the formation of amide bonds. When iron is added to the TCPP-DAP, The TCPP-DAP-Fe pattern shows the absence of the N-H group, which indicates that Fe is coordinated with N in the amide bonds and the pyridine.

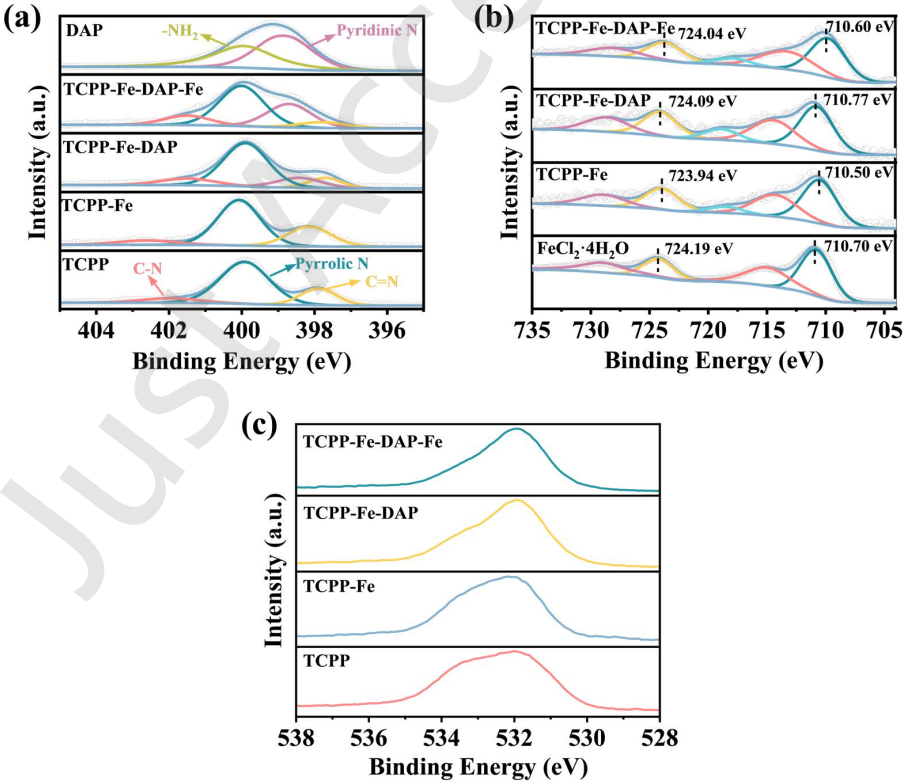

Figure S2 High-resolution (a) N 1s, (b) Fe 2p, and (c) O 1s XPS spectra of TCPP, DAP, TCPP-DAP, and TCPP-DAP-Fe.

After the introduction of Fe^{2+}, the N 1s spectrum of TCPP-Fe exhibits a pronounced shift to higher binding energy relative to TCPP. Moreover, the Fe 2p spectrum of TCPP-Fe exhibits a shift to lower binding energy, while no noticeable changes are observed in the O 1s spectra (Figure S1), indicating that Fe^{2+} preferentially interacts with the N sites in TCPP. Following the addition of DAP, TCPP-Fe-DAP exhibits a peak at 398.4 eV, corresponding to pyridinic N. Compared to TCPP-Fe, the O 1s spectrum of TCPP-Fe-DAP shows a significant change, which can be attributed to the reaction between TCPP (-COOH) and DAP (-NH_2). With the second addition of Fe^{2+}, TCPP-Fe-DAP-Fe exhibits significant changes in the N 1s peaks. In addition, the Fe 2p spectrum of TCPP-Fe-DAP-TCPP exhibits a remarkable shift, indicating that Fe^{2+} binds to the second complexation site.

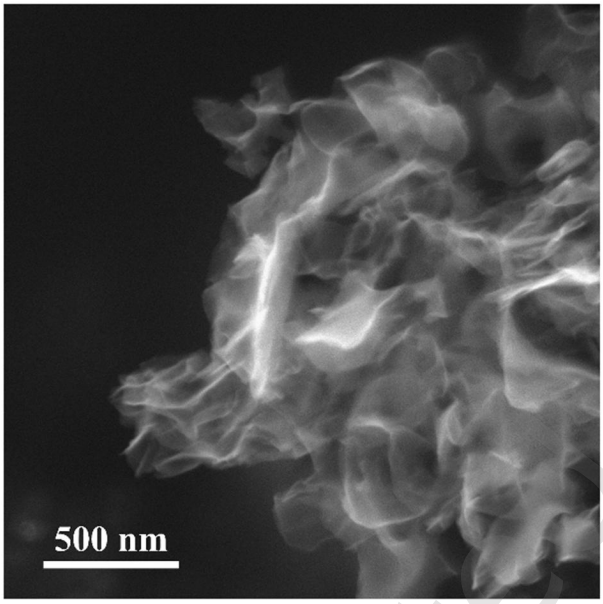

Figure S3 SEM image of DA-FeNC

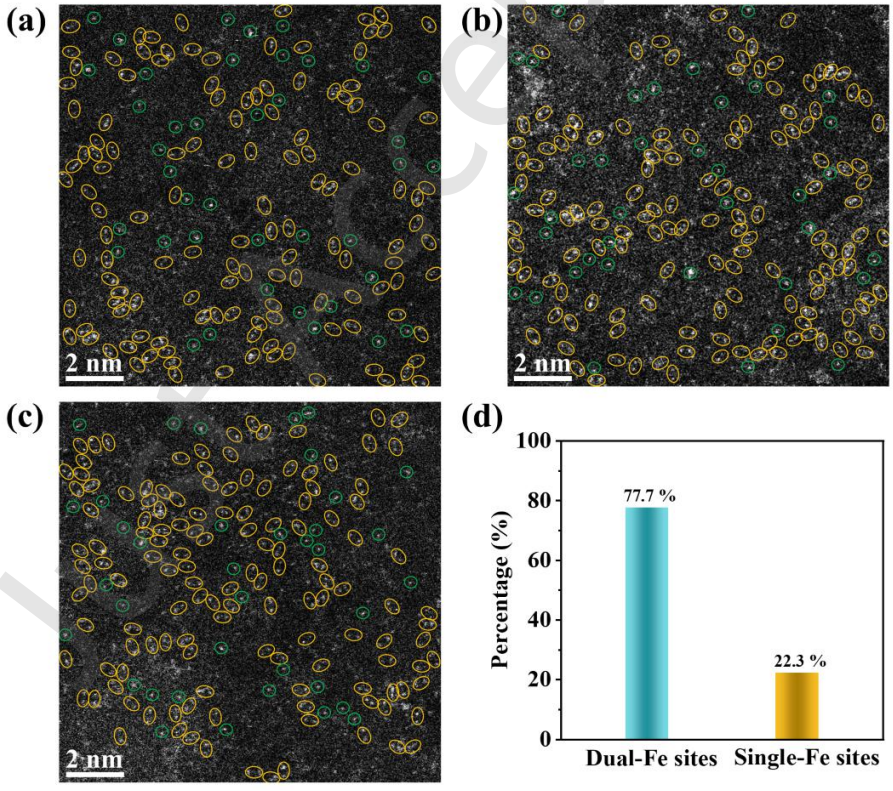

Figure S4 (a-c) HAADF-STEM images of DA-FeNC at three regions, (b) Statistical distribution (a total of 516 Fe sites) of the dual-Fe sites and single-Fe sites in (a-c)

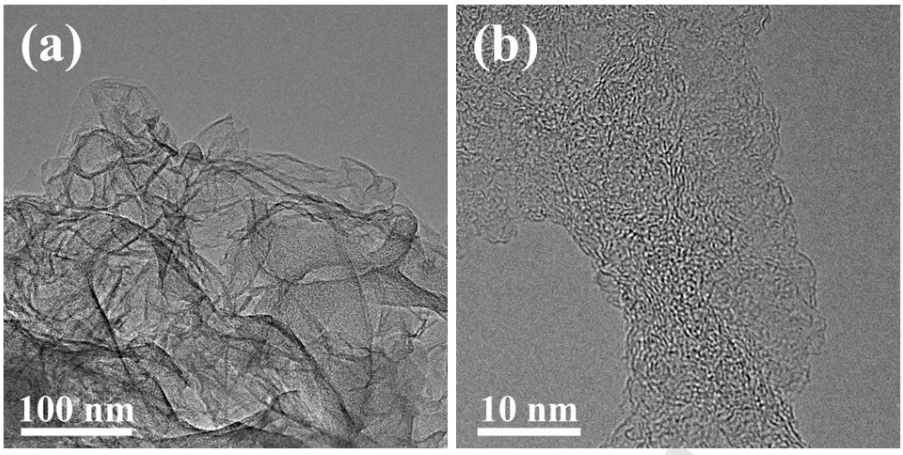

Figure S5 (a) TEM and (b) HRTEM images of SA-FeNC.

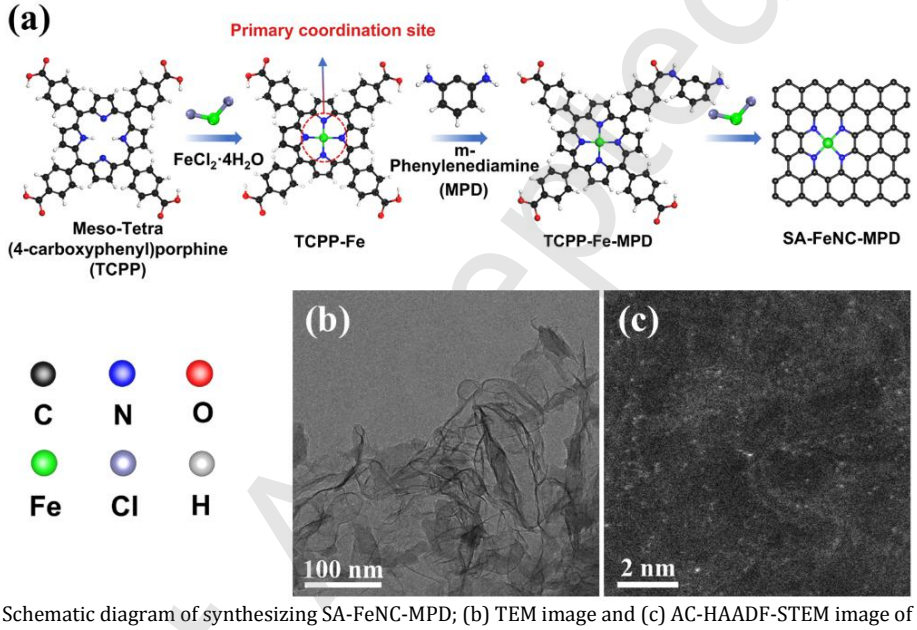

Figure S6 (a) Schematic diagram of synthesizing SA-FeNC-MPD; (b) TEM image and (c) AC-HAADF-STEM image of SA-FeNC-MPD.

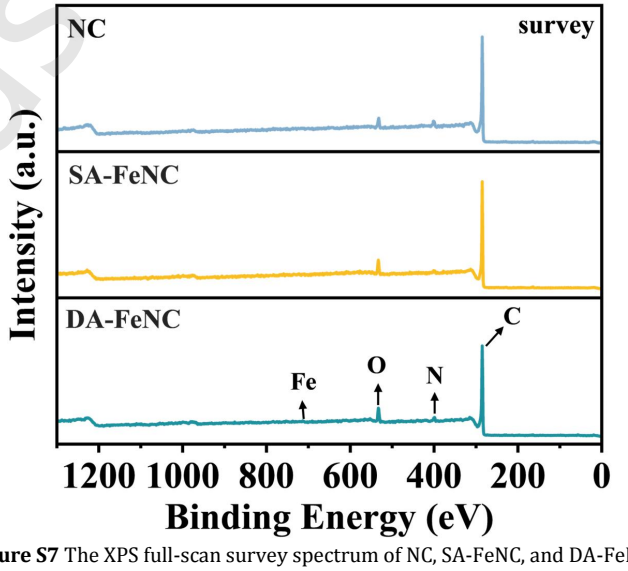

Figure S7 The XPS full-scan survey spectrum of NC, SA-FeNC, and DA-FeNC.

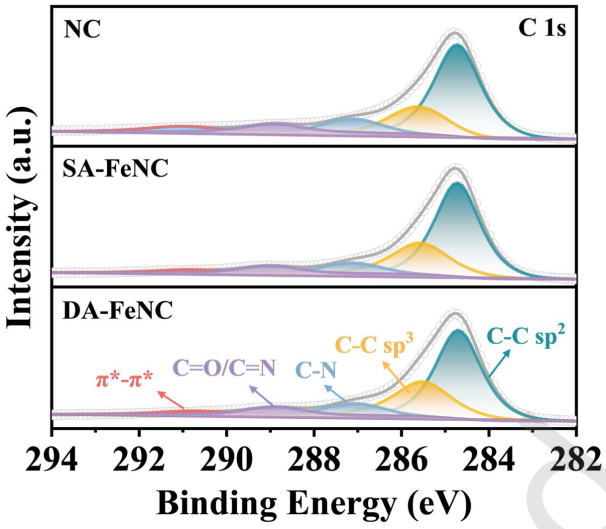

Figure S8 High-resolution C 1s XPS spectra of NC, SA-FeNC, and DA-FeNC.

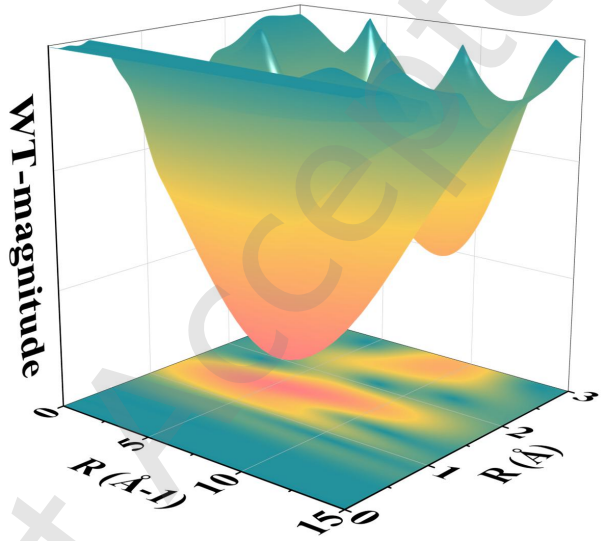

Figure S9 Wavelet transformed EXAFS of FePc

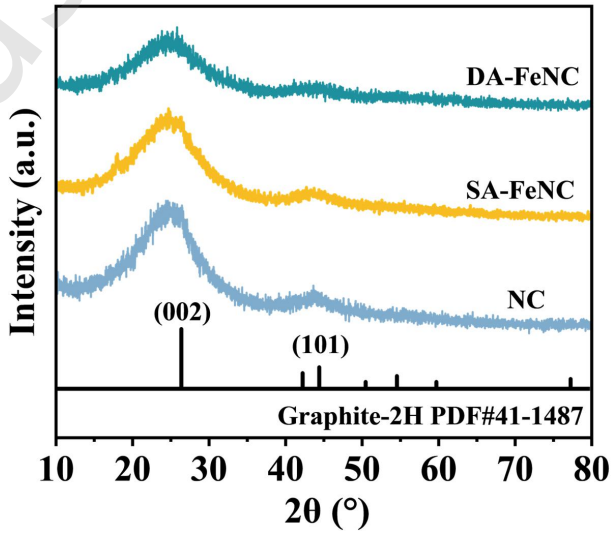

Figure S10 XRD pattern of NC, SA-FeNC, and DA-FeNC.

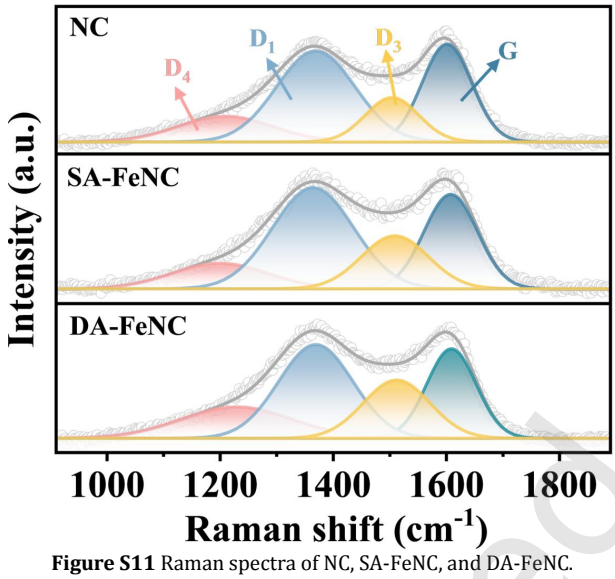

Figure S11 Raman spectra of NC, SA-FeNC, and DA-FeNC.

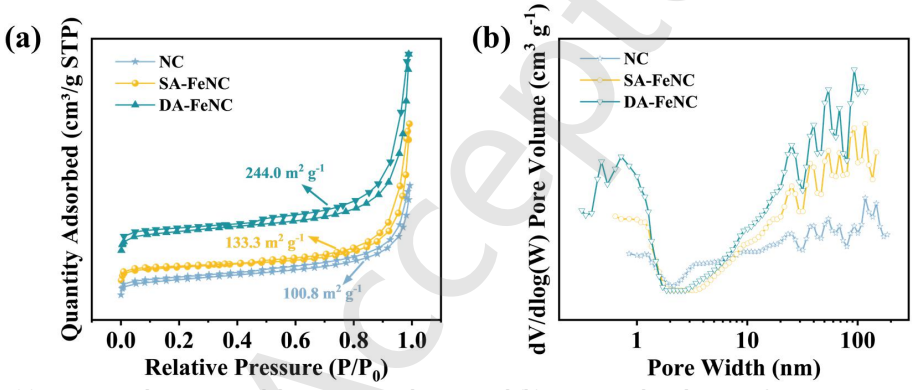

Figure S12 (a) Nitrogen adsorption and desorption isotherms, and (b) pore size distribution of NC, SA-FeNC, and DA-FeNC.

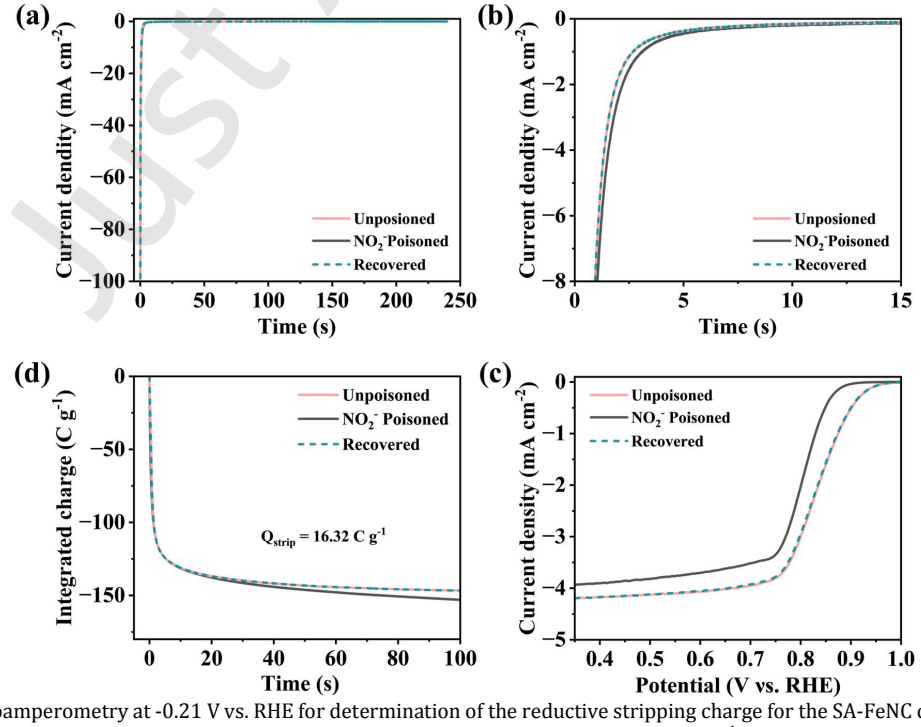

Figure S13 (a-c) Chronoamperometry at -0.21 V vs. RHE for determination of the reductive stripping charge for the SA-FeNC catalyst; (d) ORR performance of catalyst layer before, during and after nitrite adsorption. O_2-saturated electrolyte, 5 mVs^{-1} scan rate and iR-corrected rotating disk electrode experiments at 1,600 r.p.m., electrolyte: 0.5 M acetate buffer, loading: 0.27 mg cm^{-2}.

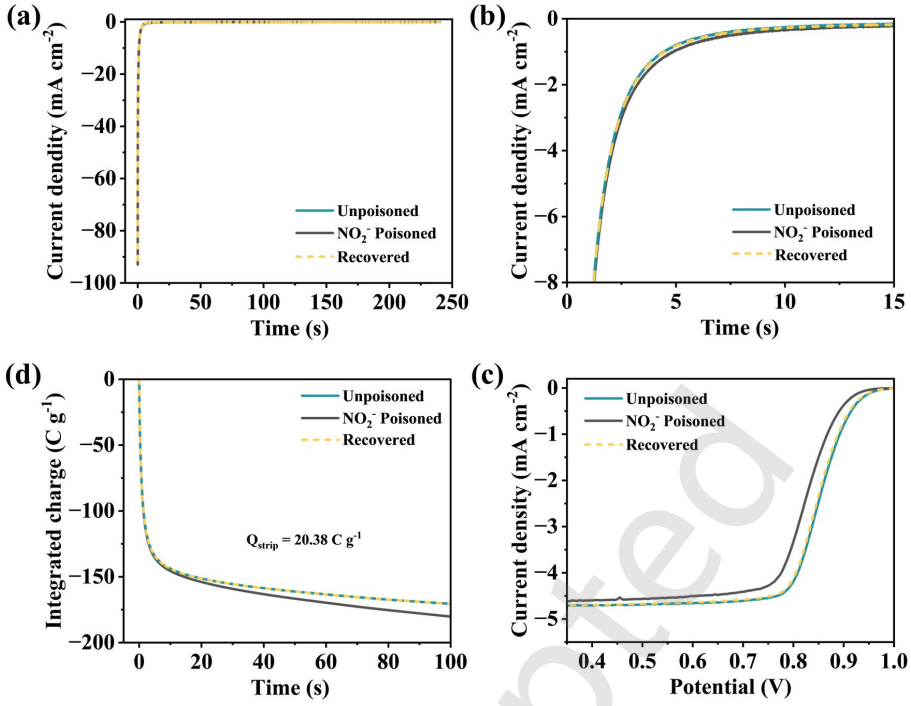

Figure S14 Chronoamperometry at -0.21 V vs. RHE for determination of the reductive stripping charge for the DA-FeNC catalyst; (d) ORR performance of catalyst layer before, during and after nitrite adsorption. O_2-saturated electrolyte, 5 mVs^{-1} scan rate and iR-corrected rotating disk electrode experiments at 1,600 r.p.m., electrolyte: 0.5 M acetate buffer, loading: 0.27 mg cm^{-2}.

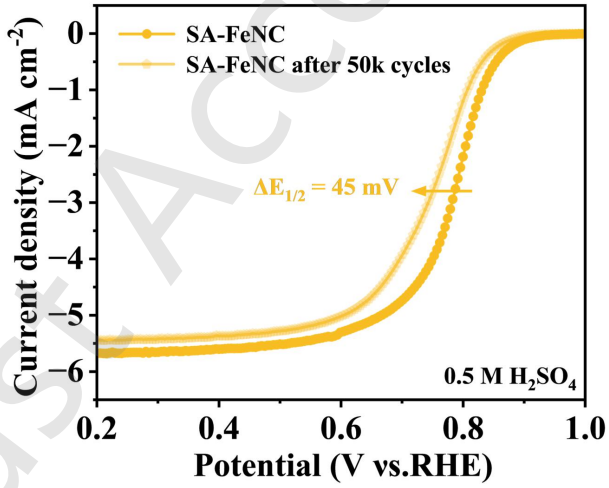

Figure S15 Cycling durability comparison of SA-FeNC in 0.5 M H_2SO_4

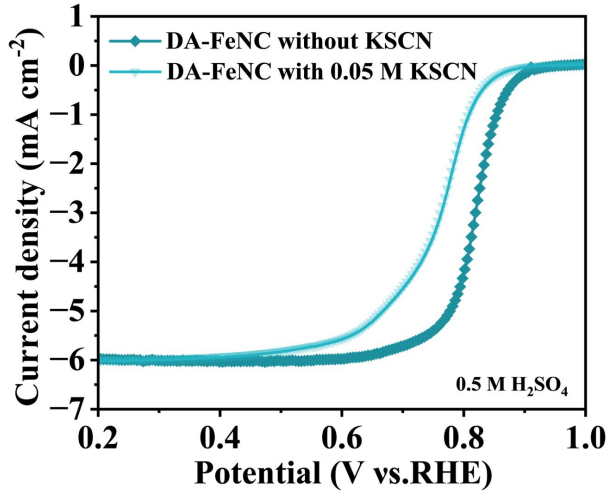

Figure S16 LSV curve of DA-FeNC catalyst in 0.5 M H_2SO_4 after the immersion of 0.05 M KSCN for 1 h

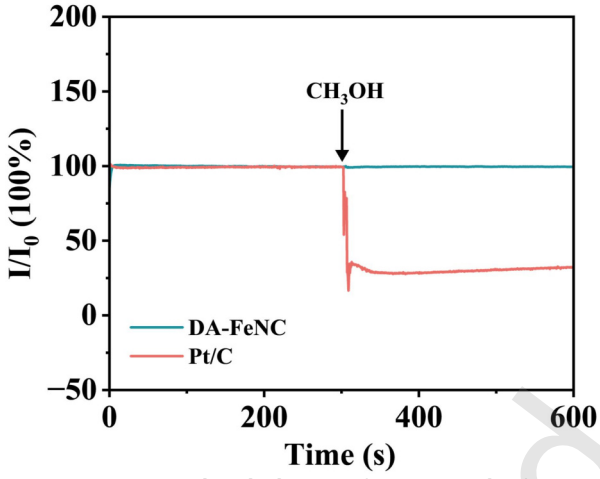

Figure S17 Methanol tolerance of DA-FeNC and Pt/C

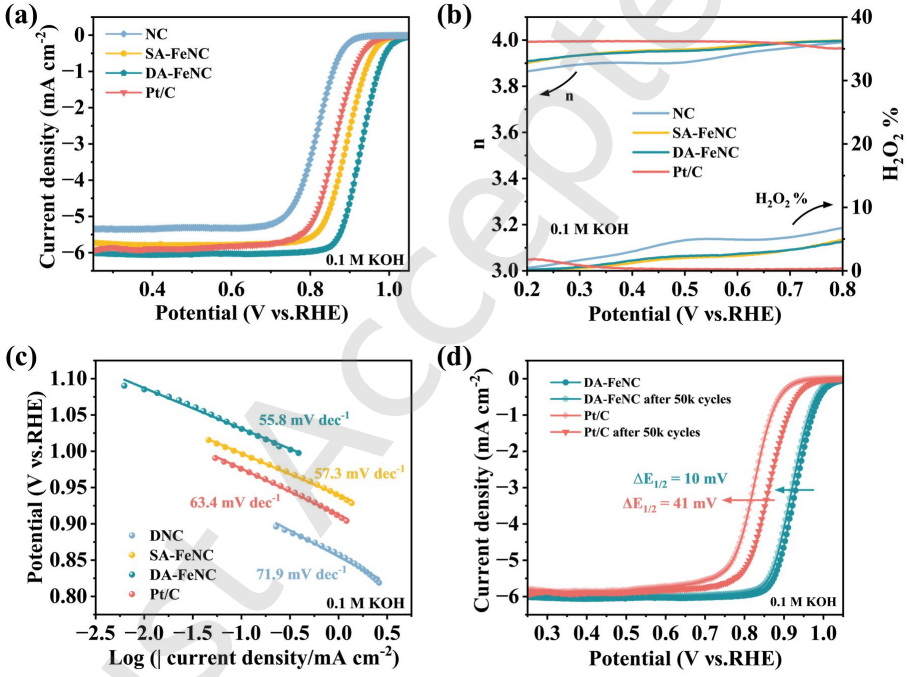

Figure S18 (a) ORR LSV polarization curves, (b) H_2O_2 yield and electron transfer number, and (c) Tafel slopes of NC, SA-FeNC, DA-FeNC, and commercial Pt/C in 0.1 M KOH; (d) Cycling durability comparison of DA-FeNC and Pt/C in 0.1 M KOH.

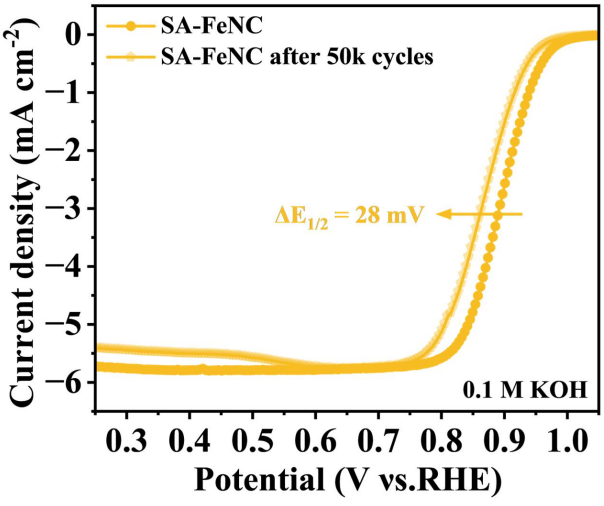

Figure S19 Cycling durability comparison of SA-FeNC in 0.1 M KOH.

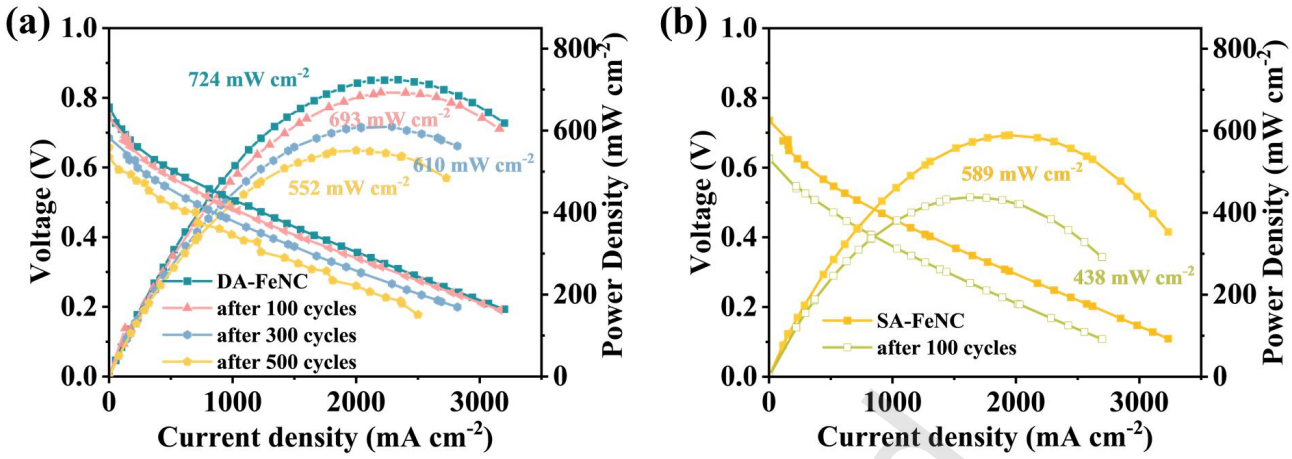

Figure S20 Cyclic-durability of (a)DA-FeNC, and (b) SA-FeNC in PEMFC.

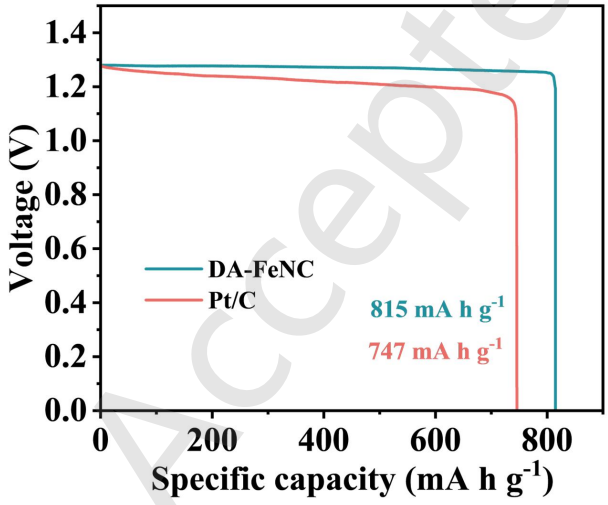

Figure S21 Specific capacities at 10 mA cm-2 for the Zn-air batteries.

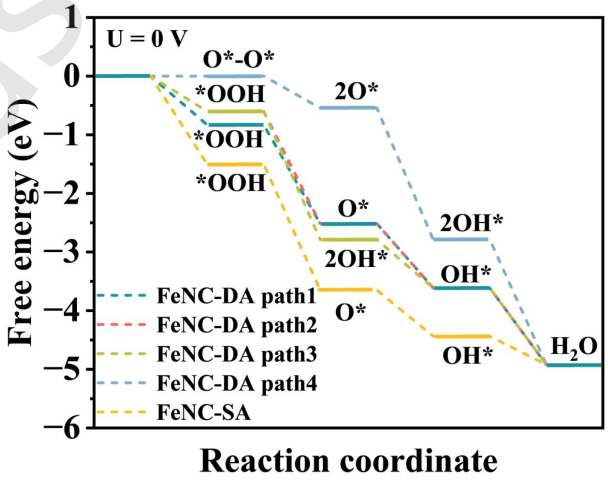

Figure S22 Free energy diagrams of DA-FeNC (four possible ORR pathways) and SA-FeNC at U = 0 eV.

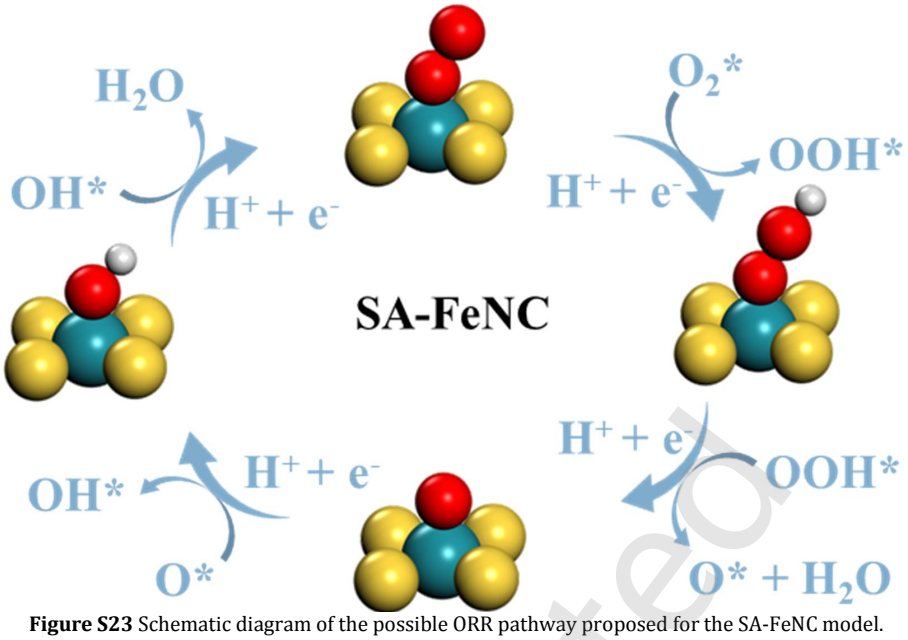

Figure S23 Schematic diagram of the possible ORR pathway proposed for the SA-FeNC model.

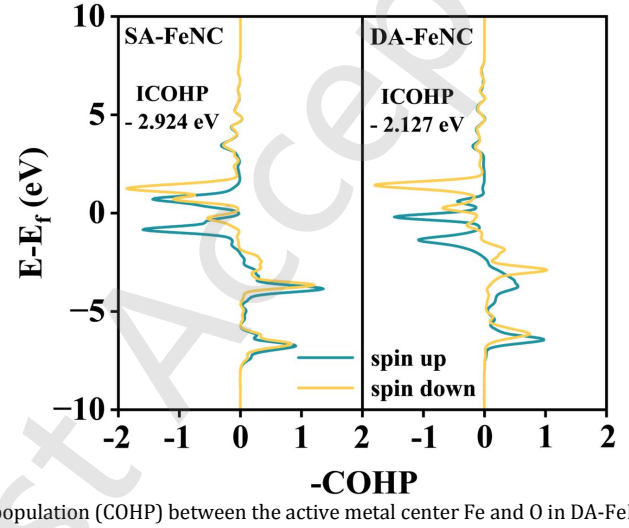

Figure S24 Crystal orbital Hamilton population (COHP) between the active metal center Fe and O in DA-FeNC and SA-FeNC after OH* adsorption.

Table S1 Summary of the elements content of samples obtained from XPS and the accurate Fe content by ICP-MS.

sample	XPS				ICP-MS
	C (at%)	N (at%)	O (at%)	Fe (at%)	Fe (wt%)
NC	90.01	4.93	5.06	-	-
SA-FeNC	89.96	2.62	7.18	0.24	1.52
DA-FeNC	87.39	4.57	7.52	0.53	2.95

Table S2. Fitting results of N 1s XPS spectra of samples

sample	Pyridinic-N (%)	Pyrrolic-N (%)	Graphitic-N (%)	Oxidized-N (%)
NC	30.60	10.91	47.53	10.96
SA-FeNC	34.50	17.80	39.29	8.41
DA-FeNC	43.77	15.11	35.78	5.34

Table S3 Fit results of Fe K-edge EXAFS for samples

sample	Path	N	R (Å)	σ^2 (Å^2)	R factor	S_0
SA-FeNC	Fe-N	4.1	1.97	0.0042	0.018	1.0
	Fe-N1	2	2.04	0.0035		
DA-FeNC	Fe-N2	2	1.93	0.0030	0.004	1.0
	Fe-Fe	1	2.58	0.0070		

Table S4 Summary of the I_{D1}/I_G and A_{D1}/A_G of samples.

sample	I_{D1}	I_G	A_{D1}	A_G	I_{D1}/I_G	A_{D1}/A_G
NC	1175	1262	204179	138572	0.93	1.47
SA-FeNC	931	868	167320	103250	1.07	1.62
DA-FeNC	1501	1345	281738	150661	1.12	1.87

Table S5 Summary of the Pore volume of samples.

sample	Micropore $cm^3 \cdot g^{-1}$	Mesoporous $cm^3 \cdot g^{-1}$	Macropore $cm^3 \cdot g^{-1}$	V total $cm^3 \cdot g^{-1}$
NC	0.03 (16.0 %)	0.09 (49.7%)	0.06 (34.3%)	0.1793
SA-FeNC	0.05 (16.6%)	0.12 (43.8%)	0.10 (38.6%)	0.2700
DA-FeNC	0.09 (24.9%)	0.16 (44.5%)	0.11 (30.6%)	0.3624

Table S6 Summary of the Q_{strip}, SD_{mass}, TOF, and J_k of samples

sample	Q_{strip} (C g^{-1})	SD_{mass} (sites g^{-1})	TOF (e $site^{-1}$ s^{-1})	J_k (mA cm^{-2})
NC	-	-	-	**0.03**
SA-FeNC	16.32	2.04×10^{19}	4.62	1.02
DA-FeNC	20.38	2.54×10^{19}	2.92	0.50

Table S7 The ICP-MS after 50,000 cycles in 0.5 M H_2SO_4.

Sample	ICP-MS	Leaching ratio
DA-FeNC	9.77 μg L^{-1}	25.3%
SA-FeNC	19.05 μg L^{-1}	6.67%

Table S8 The number of d orbital electrons in the PDOS of DA-FeNC and SA-FeNC

sample	d_{xy}	d_{yz}	d_{xz}	d_{z^2}	$d_{x^2-y^2}$	total
DA-FeNC	1.33	1.45	1.39	1.34	0.95	6.46
SA-FeNC	1.83	1.06	1.60	0.99	0.84	6.32

Table S9 The ICOHP value of Fe (d_{xy}, d_{yz}, d_{xz}, $d_{x^2-y^2}$, and d_{z^2})-O (p_x, p_y, p_z) of the Fe-O bond in OH*

Model	DA-FeNC	SA-FeNC
Fe - O	**-2.12653**	**-2.92419**
Fe $3d_{xy}$ - O $2p_y$	-0.00595	-0.00102
Fe $3d_{xy}$ - O $2p_z$	-0.00007	-0.00006
Fe $3d_{xy}$ - O $2p_x$	0.00006	-0.00007
Fe $3d_{yz}$ - O $2p_y$	-0.29359	-0.38371
Fe $3d_{yz}$ - O $2p_z$	-0.00279	-0.01083
Fe $3d_{yz}$ - O $2p_x$	-0.00559	-0.00025
Fe $3d_{z^2}$ - O $2p_y$	0.00057	-0.0029
Fe $3d_{z^2}$ - O $2p_z$	**-0.72913**	**-1.15553**
Fe $3d_{z^2}$ - O $2p_x$	0.00576	-0.04169
Fe $3d_{xz}$ - O $2p_y$	-0.00456	-0.00048
Fe $3d_{xz}$ - O 2pz	-0.05341	-0.0041
Fe $3d_{xz}$ - O $2p_x$	-0.07911	-0.06986
Fe $3d_{x^2-y^2}2$ -O $2p_y$	-0.00043	-0.00027
Fe $3d_{x^2-y^2}$ - O $2p_z$	-0.00329	-0.00003
Fe $3d_{x^2-y^2}$-O $2p_x$	-0.00118	-0.00075

Table S10. Summary of ORR performance of dual-atom Fe-N-C in acidic media

Catalysts	Distances of dual atoms		DFT model	Synthetic method	$E_{1/2}$ (V vs. RHE) Electrolyte	$E_{1/2}$ loss / mV Cycles	References
	AC-HAADF-STEM	EXAFS					
DM-FeNC	**2.64 Å /2.73 Å**	**2.58 Å**	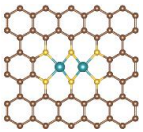 **Fe-N-Fe**	**A newly binuclear ligand amide polymer**	**0.82 0.5 M H_2SO_4**	**26 50k**	**This work**
Fe_2N_6-S	2. 5 Å	2.53 Å	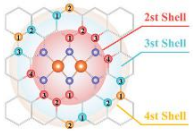 Fe-N-Fe	Biomimetic dual Fe precursor and host-guest encapsulation.	0.783 0.5 M H_2SO_4	-	Adv. Mater. 36, 2309231 (2024)
Fe, Cu DAs-NC	4.1 Å	-	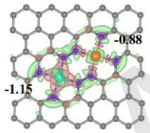 Fe-N_2-Fe	FePc Host-guest encapsulation and defects engineered around FeN_4 sites.	0.80 0.5 M H_2SO_4	-	Energy Storage Mater. 54, 533-542 (2023)
PtFe-DAC	2.57 Å	2.6 Å	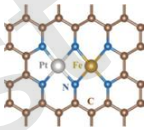 Fe-N-Pt	π-π stacking and electrostatic assembly of Pt-Fe diatomic sites on ZIF-derived NC	0.785 0.1 M $HClO_4$	-	Adv. Funct. Mater. 34 , 2407128 (2024)
Fe_2-S_1N_5/SNC	2.46 Å	2.46 Å	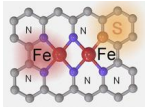 Fe-N-Fe	Bis(dicarbonylcyclopentadienyliron) (CDD) as the precursor.	0.829 0.1 M $HClO_4$	26 5k	Energy Environ. Sci. 17, 4646-4657 (2024)
T-Fe-N-C	2.5 Å	2.52 Å	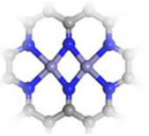 Fe-N-Fe	Atmosphere-induced single- to dual-atom sites conversion.	0.88 0.1 M $HClO_4$	90 80k	Angew. Chem. Int. Ed. 64, e202510671 (2025)

FeCu-NC	2.3~2.4 Å	2.4 Å	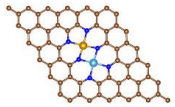 Fe-N-Cu	Host-guest encapsulation.	0.805 0.1 M $HClO_4$	-	Energy Environ. Sci. 18, 7624-7634 (2025)
Fe_2N_6	-	2.47 Å	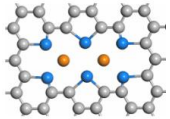 Fe-N-Fe	Temperature-driven single- to dual-atom sites.	0.84 0.1 M $HClO_4$	24 10k	Matter 3, 509-521 (2020)
(FeMn-DA)-N-C	2.34 Å	2.5 Å	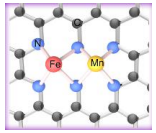 Fe-N-Mn	host-guest encapsulation (ZIF-8)	0.82 V 0.1 M $HClO_4$	14 mV 5k	Nano-Micro Lett. 17, 88 (2025)
MnFe-PNC	4.8 Å	-	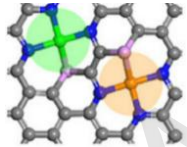 Fe-N-C-P-Mn	host-guest encapsulation.	0.803 0.1 M $HClO_4$	14 mV 5k	Adv. Mater. 37 41, e14343 (2025)
Fe-Co DACs	2.22~2.28 Å	2.50 Å	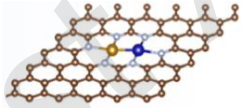 Fe-Co	Molecular chelation and ionic coupling.	0.852 0.5 M H_2SO_4	15 10k	Nat. Commun. 16, 7198 (2025)
Fe_2-DAC	-	-	-	Encapsulation-pyrolysis Approach.	0.79 0.1 M $HClO_4$	11 10k	J. Am. Chem. Soc. 145, 4819-4827 (2023)
FeCo-3DMNC	-	-	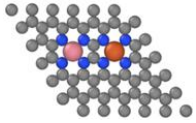 Fe-N-C-N-Co	ZIF-8-derived ion-exchange method	0.806 0.5 M H_2SO_4	19 10k	Adv. Energy Mater. 15, 2404140 (2024)

Fe_2@PDA-ZIF-900	2.2 Å	2.41 Å	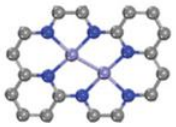 Fe-Fe	Fe dimer as the precursor.	0.817 0.5 M H_2SO_4	a negligible change 5k	Adv. Funct. Mater.32, 2205637 (2022)
FeAl-RNC	2.3 Å	2.3 Å	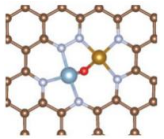 Fe-O-Fe	Multi-step polymerization pyrolysis.	0.83 0.5 M H_2SO_4	16 10k	J. Am. Chem. Soc.146, 12636-12644 (2024)
Mn-Fe/p-DC-900	-	-	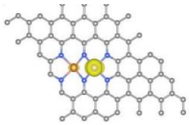 Fe-N-Mn	Mn-doped ZIF + resorcinol-formaldehyde coating + Fe^{3+} incorporation	0.80 0.5 M H_2SO_4	20 5k	Adv. Energy Mater. 14, 2400368 (2024)
Fe-Co-NC	2.09 Å	2.29 Å	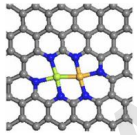 Fe-Co	Biopolymer-coated Fe-Co Prussian blue analogue	0.729 0.5 M H_2SO_4	-	Adv. Funct. Mater. 34, 2408257 (2024)
Fe_2-S/NC-6	-	2.38 Å	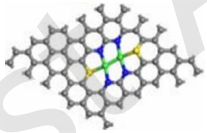 Fe-Fe	Pre-synthesized Prussian blue analogue as a precursor.	0.78 0.5 M H_2SO_4	29 8k	Small Methods. e01359 (2025)
Fe_2N_5	-	2.12 Å	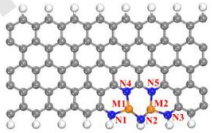 Fe-N-Fe	ZIF-8-derived ion-exchange method	0.82 0.1 M $HClO_4$	-	J. Am. Chem. Soc.141, 17763-17770 (2019)

Table S11. Summary of ORR performance of dual-atom Fe-N-C in alkaline media

Catalysts	Distances of dual atoms		DFT model	Synthetic method	$E_{1/2}$ (V vs. RHE) Electrolyte	$E_{1/2}$ loss / mV Cycles	References
	AC-HAADF-STEM	EXAFS					
DM-FeNC	**2.64 Å /2.73 Å**	**2.58 Å**	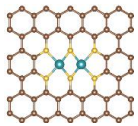 **Fe-N-Fe**	**A newly binuclear ligand amide polymer**	**0.93 0.1 M KOH**	**10 50k**	**This work**
Fe-DPs/NC	2.9 Å	3.05 Å	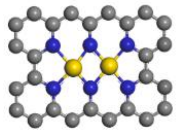 Fe-N-Fe	Bis(dicarbonylcyclopentadienyliron) (CDD) as the precursor.	0.90 V 0.1 M KOH	-	Chem. Eng. J. 506, 159888 (2025)
DiFe-N/CBs	2.1 Å	3.04 Å	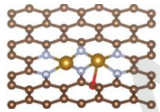 Fe-N-Fe	Ligand confined combining the cation-exchange of dimeric metal complex .	0.91 0.1 M KOH	30 50k	Angew. Chem. Int. Ed. 64, e202413933 (2025)
Fe_2-pPc	2.55 Å	2.58 Å	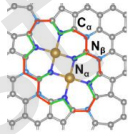 Fe-N-Fe	Cohesion of adjacent Fe-N_x fragments.	0.92 0.1 M KOH	17 150k	J. Am. Chem. Soc. 146, 24842-24854 (2024)
Fe_2/NC	2. 8 Å/ 3.0 Å	3.04 Å	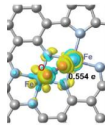 Fe-N-Fe	A sublimation transformation.	0.90 0.1 M KOH	a negligible change 10k	Angew. Chem. Int. Ed. 64, e202413179 (2024)
Fe_2N_6-S	2.5 Å	2.53 Å	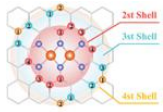 Fe-N-Fe	Biomimetic dual Fe precursor and host-guest encapsulation.	0.921 0.1 M KOH	a negligible change 5k	Adv. Mater. 36, 2309231 (2024)

$Fe-N_2-Fe$	2.9 Å	-	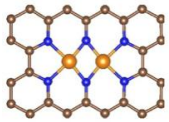 Fe-N-Fe	Electrostatic interaction control and neighboring vacancy construction	0.91 0.1 M KOH	4 40k	Angew. Chem. Int. Ed. 63, e202408914 (2024)
Fe_2N_6	-	2.53 Å	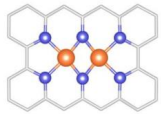 Fe-N-Fe	Fe dimer precursor and host-guest encapsulation.	0.912 0.1 M KOH	-	Adv. Mater. 36, 2309231 (2024)
$FeCo-N_3O_3@C$	2.52 Å	2.52 Å	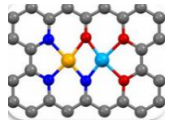 Fe-N-Co; Fe-O-Co	Defects engineered around FeN_4 sites.	0.936 0.1 M KOH	9 10k	Nat. Synth. 3, 878-980 (2024)
FeDy-DAC	3.0 Å	2.988 Å	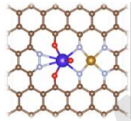 Fe-N-Dy	impregnation and adsorption method	0.90 V 0.1 M KOH	-	Adv. Mater. 38, e20359 (2026)
Fe_2-NC-850	2.23±0.5 Å	2.60 Å	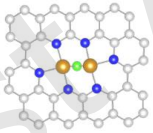 Fe-Cl-Fe	Fe_2Cl_6 dimers	0.887 V 0.1 M KOH	14 mV 20k	J. Am. Chem. Soc. 148, 665-676 (2026)
FeMn-N-C	-	-	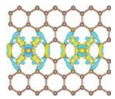	The electrospinning-pyrolysis-etching route.	0.92 0.1 M KOH	19 50k	Adv. Mater. 2405763 (2024)
Fe_2-N_6	2.9 Å	2.62 Å	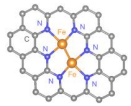 Fe-Fe	Interfacial-fixing strategy.	0.90 0.1 M KOH	10 50k	Nat. Commun. 16, 334 (2025)

Fe_2DAC	2.23 Å	2.556 Å	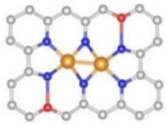 Fe-N-Fe; Fe-Fe	A hollow-structured COF with preorganized bimetallic chelating sites.	0.898 0.1 M KOH	-	Angew. Chem. Int. Ed. 62, e202304412 (2023)
FeCo-N/P-C	2.5 Å	2.47 Å	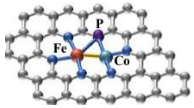 Fe-P-Co; Fe-Co	Pre-screened bimetallic precursors	0.913 0.1 M KOH	4 30k	Nat. Commun. 16, 8111 (2025)
Fe/Co-SAs-N_x-PCNSs	-	-	-	ZIF spatial confinement strategy	0.90 0.1 M KOH	-	Nano Res. 16, 11464-11472 (2023)
Fe_{SA+AC}-N/Se-AHCs	-	1.91 Å	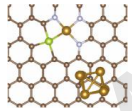	Template-assisted self-assembly	0.90 0.1 M KOH	3 9k	App. Catal. B: Environ. 383， 126102 (2026)
FeCo-N-C-1.25	2.63 Å	2.39 Å	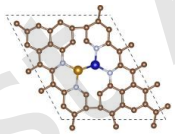 Fe-Co	Increasing the amount of metal precursors.	0.853 0.1 M KOH	19 5k	Angew. Chem. Int. Ed. e202419595 (2024)
CoNP@FeNC-0.05	-	-	-	ZIF-8 “double solvents” method	0.85 0.1 M KOH	40 5k	Nano-Micro Lett. 14, 162 (2022)
c-FeCoDAC	5.1 Å	-	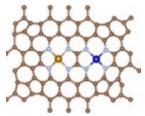 Fe-N-C-Co	ZIF spatial confinement strategy	0.85 V 0.1 M KOH	5 mV 3k	Angew. Chem. Int. Ed. e21225 (2026)